

1

2

3

Contents

4	0.1	Introduction	1
5	0.1.1	Historical retrospective	1
6	0.1.2	Actual challenges	2
7	0.1.3	Thesis composition	3
8	1	The Standard Model	5
9	1.1	General composition and key parameters	5
10	1.2	Classical fields and gauge invariance principle	8
11	1.3	Quantum electrodynamics	10
12	1.4	Electroweak theory and the Higgs mechanism	12
13	1.4.1	Electroweak gauge fields	12
14	1.4.2	Fermion sector	12
15	1.4.3	Higgs fields breaking the symmetry	13
16	1.4.4	Physical interpretation of gauge fields and parameters	14
17	1.5	Chromodynamics	15
18	2	The W boson	19
19	2.1	Introduction	19
20	2.2	W boson production at the LHC	19
21	2.3	W boson decay	19
22	2.4	W boson detection	19
23	2.5	Precision measurements of $W pT$	19
24	2.6	Precision measurements of W mass	19
25	3	The Large Hadron Collider	21
26	3.1	Introduction	21
27	3.2	The LHC running sequence	21
28	3.3	Special low pile-up run during LHC Run 2	25
29	4	The ATLAS detector	27

30	4.1 General description and layout	27
31	4.2 Coordinate system	27
32	4.3 Magnet system and magnetic field	28
33	4.4 Inner detector	28
34	4.5 Calorimeter system	30
35	4.5.1 Electromagnetic calorimeter	31
36	4.5.2 Hadronic calorimeter	34
37	4.6 Muon detectors	35
38	4.7 Forward detectors	37
39	4.8 Trigger system	39
40	5 Electromagnetic shower shapes correction in the electromagnetic calorimeter	41
41	5.1 Introduction	41
42	5.2 Shower shapes measurement and correction	44
43	5.2.1 Event selection	44
44	5.2.2 Data/MC discrepancies	44
45	5.2.3 The correction procedure	46
46	5.3 Results	47
47	5.4 Appendix: control plots	48

48

List of Figures

49	11 The list of particles that enters the Standard Model (SM)[sm_wiki].	7
50	12 The evolution of the SM running coupling constants [coupl_wiki].	8
51	13 The QEQ diagrams: Compton scattering, electron self-energy, photon self-energy.	11
52	14 Electroweak sector and the Weinberg rotation [coupl_wiki].	16
53	15 The formation of a jet [conf_wiki].	17
54	31 A Toroidal LHC ApparatuS (ATLAS) A hydrogen tank supplies LHC with protons [hydro].	22
55	32 Schematic depiction of the LHC ring.	23
56	33 Bunching at RF cavities	23
57	34 The crossing	24

58	35	Number of Interactions per bunch crossing in ATLAS Run 2 [run2lumi]. A little bump around $\mu \approx 2$ corresponds to special low pile-up runs.	26
60	41	ATLAS detector general layout	28
61	42	Geometry of ATLAS magnet windings	29
62	43	Fichier Gerber des modèles d CFR-34 et CFR-35.	30
63	44	ATLAS calorimeter general layout	31
64	45	ATLAS EM calorimeter layers	33
65	46	Accordion absorbers of the electromagnetic calorimeter (EMC)	34
66	47	ATLAS muon system	35
67	48	Cut views of the muon systems	37
68	49	ATLAS forward detectors	39
69	410	The scheme of ATLAS trigger systems	40
70	51	The schematic portrayal of EM shower development	41
71	52	Visualisations of the 7x11 calorimeter cluster	42
72	53	Shower shapes in the second layer of the electromagnetic calorimeter	42
73	54	Distribution of R_η in simulation (GEANT4) for electrons and jets [sshapes_simulation].	43
74	55	Data/MC Comparison for Calorimeter Shower Shapes of High Et Electrons [geant_corr].	44
75	56	R_η in the barrel and in the end-cap, Data vs MC	45
76	57	R_ϕ in the barrel and in the end-cap, Data vs MC	45
77	58	W_η^2 in the barrel and in the end-cap, Data vs MC	46
78	59	R_ϕ in the barrel and in the end-cap, Data vs MC	47
79	510	Schematic energy profile in ϕ dimension. Bremsstrahlung tails subtraction based on e^+ and e^- energy profiles.	47
81	511	R_η in the barrel and in the end-cap	48
82	512	R_ϕ in the barrel and in the end-cap, Data, MC, reweighted MC	49
83	513	W_η^2 in the barrel and in the end-cap, Data, MC, reweighted MC	49
84	514	Distributions integrated over pT (a) R_ϕ ; (b) R_η ; (c) $W_{\eta 2}$	50
85	515	Electron identification efficiency as a function of the electron pseudo-rapidity	50
86	516	Reta 2	51
87	517	Rphi in all eta slices	52
88	518	Reta 2	53
89	519	Reta 2	54
90	520	Reta 2	55
91	521	Reta 2	56

92	522	Reta 2	57
----	-----	------------------	----

93

List of Tables

94	41	ATLAS calorimeter in numbers	32
95	42	ATLAS muon spectrometer subsystems coverage and parameters	38

⁹⁶ 0.1 Introduction

⁹⁷ 0.1.1 Historical retrospective

⁹⁸ The reductionistic idea that all the countless variety of matter types that surrounds us could be in fact
⁹⁹ brought to a combination of much fewer substances has been around at least since the time of Ancient
¹⁰⁰ Greece. A thought that you can construct everything you see around out of one or few (e.g. fire, earth,
¹⁰¹ water and air) indivisible elements ($\alpha\tauομοζ$ in greek) is simple, logical and therefore conceptually
¹⁰² attractive. Knowing all about these elements could potentially grant us profound understanding
¹⁰³ of nature. But it wasn't before the XIX century when this idea has become something more than a
¹⁰⁴ philosophical concept and obtained solid scientific evidence.

¹⁰⁵ The composition of the periodic table of elements in 1860s [1] was a tremendous step forward, reducing
¹⁰⁶ the number of elements to O(100). The elements of the periodic table resembled the ancient greek
¹⁰⁷ concept so much, that they were christened atoms. But the periodic character of the table and strong
¹⁰⁸ correlation of atom position in the table with its chemical properties was insinuating on a certain inner
¹⁰⁹ structre of the atoms, a possibility for them to be composed out of even smaller objects. The discovery
¹¹⁰ of isotopes in 1913 [2] left little room for other explaination.

¹¹¹ Further evidences in favor of atomistic views kept coming in late XIX and early XX centuries from
¹¹² theoretical and experimental sides. The molecular kinetic theory has been heavily critisized throughout
¹¹³ the XIX century, but the explaination of the brownian motion [3] has secured its dominance from there
¹¹⁴ on lying a foundation for what is to become the statistical physics. Of particular importance was the
¹¹⁵ discovery of the first subatomic particle in 1897, which was called the electron [4].

¹¹⁶ Further studies of radioactive materials have allowed to compose a seemingly consistent understanding
¹¹⁷ of what matter is composed of. By the time of neutron discovery in 1932 [5] the list of what was called
¹¹⁸ elementary particles was reasonably short: an electron, a proton, and a neutron. It was still left to figure
¹¹⁹ out how these elements interact forming the known atoms, moleculas and all the matter around. That
¹²⁰ required additional efforts on the theoretical side, including resolving the inconsistencies between the
¹²¹ two new branches of physics supposed to describe the microworld and the fields, namely the quantum
¹²² theory and the field theory.

¹²³ To move forward the physicist have made use of another source of elementary particles - the cosmic
¹²⁴ rays. Cosmic rays contained particles of much higher energies comparing to the radioactive materials.
¹²⁵ Cosmic ray experiments have led to the discovery of the first known antiparticle - the positron [6],
¹²⁶ confirming the theoretical predictions by Dirac [7]. Further discoveries of the muon [8], pion [9], kaon
¹²⁷ [10] and Λ_0 [11] have shown that the list of elementary particles was still far from being completed.
¹²⁸ The second half of the XX century has pronounced a new era in particle physics with the extensive use
¹²⁹ of particle accelerators. Accelerators have become the main experimental tool in the discovery of new
¹³⁰ particles and investigation of their properties. Comparing to the cosmic rays, accelerators could offer
¹³¹ higher energies and better control over the experimental conditions. Thanks to these new tools by the
¹³² end of 1960s the number of newly discovered particles has exceeded one hundred and kept growing,

133 apparently taking away the reductionistic dream of having a reasonably small number of elementary
134 particles.
135 On the other hand, the properties of the newly discovered particles (sometimes called "the particle
136 zoo") had provided enough experimental data for theorists to make further assumptions. The particles,
137 if grouped by their properties, have formed patterns - a situation resembling the old story with the
138 atoms of the periodic table. This observation has allowed to assume the existence of even smaller
139 fundamental particles with a fractional charge that would make up all the visible hadrons. These
140 particles were eventually called quarks [12], [13]. By the late 1960s hypothesising the existence of
141 only three quarks was enough to explain all the visible particles and successfully predict new ones [14].
142 Since then three more quarks were discovered and as of now all the experimental evidence suggests
143 that the quarks are truly fundamental particles being indivisible in the Ancient Greek sense.
144 At the same time serious theoretical efforts were taken in order to describe the interactions between
145 fundamental particles, taking into account the known fundamental forces. In the mid-1970s a theory
146 called The Standard Model was finalized. It included three out of four known fundamental forces
147 (excluding the gravity) and predicted a number of particles which were not discovered by that time.
148 All the key predictions of the theory were successfully confirmed by further experiments, making it a
149 dominant theory in particle physics. The theory was able to describe all the surrounding matter with
150 only 12 fundamental fermions (and their antiparticles) and 5 bosons. The SM is described in more
151 detail in the Chapter 1.
152 Theoretical efforts aimed to further simplify the list of fundamental particles are ongoing, but up to
153 the time of this thesis writing none of them were confirmed experimentally.

154 **0.1.2 Actual challenges**

155 The establishment of the Standard Model was a colossal step forward in understanding of the mi-
156 croworld physics. Nevertheless despite its great success and very good agreement with vast majority of
157 the experimental data there is a number inconsistencies and lacunas in the theory, which do not allow
158 to think of the SM as of the final theory. Here are most notable of these problematic questions:

- 159 1. A number of neutrino experiments have established that the neutrinos have a tiny though non-
160 zero mass. The minimal Standard Model assumes neutrinos to be massless and does not allow to
161 provide mass to the neutrinos.
 - 162 2. Astrophysical and cosmological evidences confirm the existence of the dark matter which does
163 not correspond to any of the SM particles.
 - 164 3. Cosmological observations show a substantial disproportion between observed matter and anti-
165 mater in favor of the former. The SM does not provide an explanation how such an imbalance
166 could have been formed.
-

167 4. The discovery of the gravitational waves in 2016 had confirmed the existence of the graviton - the
168 mediator of the gravitational force. The gravitational force is not represented in any way in the
169 SM.

170 5. No explanation is provided to the vastly different magnitude of the fundamental forces, i.e. why
171 the gravity is 10^{24} times weaker than the weak force.

172 In order to attack these and other problems numerous efforts have been taken to either modify
173 the SM or to replace it with a more fundamental theory, but so far none of these Beyond Standard
174 Model (BSM) theories were ever confirmed experimentally. The SM is still a source of most accurate
175 predictions for any physical process that involves elementary particle interactions. Description of the
176 BSM theories goes beyond the scope of current thesis.

177 The SM depends on the list of 18 free parameters (to be described in more detail in Chapter 1). These
178 parameters can not be calculated intrinsically and must be measured experimentally. The more precisely
179 we know the values of these parameters - the better is the accuracy of the SM prediction. Precise
180 knowledge of the SM input parameters can also give hints on where to look for a more fundamental
181 theory.

182 The LHC experiments have already contributed greatly by discovering the last missing piece of the SM,
183 the Higgs boson. This has ended the era of SM particle discoveries but at the same time started the era
184 of LHC precision measurements. The LHC experiments were capable to measure some parameters
185 of the SM for the first time (like the mass of the Higgs boson), but also could improve the existing
186 measurements, boosting the predictive power of the SM.

187 This thesis is a part of an ongoing effort at the ATLAS experiment to improve the precision of the W
188 boson mass, which is also among the SM free parameters. The mass of the W boson was first measured
189 at Large Electron-Positron (LEP) after its discovery in 1983. The precision of the measurement was
190 further improved by the experiments at Tevatron collider. The only LHC result performed so far was
191 published by ATLAS collaboration in 2018.

192 Hadron colliders are a challenging environment for the W boson-related measurements, the precision
193 is highly impacted by a number of factors one of them being the pile-up. Current analysis is based on
194 the data collected during two special LHC runs with low pile-up, takein in 2017 and 2018.

195 0.1.3 Thesis composition

196 The first chapter contains the description of the Standard Model, its constituents and input parameters.
197 Chapter 2 is dedicated to W boson and its properties. Chapter 3 tells about the Large Hadron Collider
198 (LHC) and its operations. ATLAS detector is discribed in Chapter 4. Chapter 5 is dedicated to the
199 description of the shower shapes reweighting. And so on and so forth...

200

201

1

The Standard Model

202 *"Potentielle citation sans aucun rapport avec le sujet"*

203 — Personne inconnue, contexte à déterminer

204 The SM of particle physics is a quantum field theory that postulates the existence of three generations
205 of quarks and leptons interacting through three fundamental forces: electromagnetic, weak and strong.
206 From the mathematical point of view the SM is a gauge quantum field theory that has internal sym-
207 metries of the unitary product group $SU(3) \times SU(2)_L \times U(1)$. The fourth fundamental force, namely
208 the gravity, is not included in the SM. Nevertheless, since the magnitude of the gravity interaction is
209 negligible on the microscopic scale, it has little to no effect on the precision of the SM predictions. The
210 model has 18¹ free input parameters - the physical constants that can not be predicted from within
211 the theory and must be measured experimentally. Evidently, the SM predictions are based on these
212 parameters, so the better we know them - the better we can predict how nature behaves on the micro-
213 level. The free parameters of the SM are briefly described in section 1.1

214

215 A comprehensive description of the quantum field theory formalism goes beyond the scope of
216 current dissertation and can be found in the corresponding textbooks [1], [2], [3], [4], [5], [6]. In the
217 following sections a brief overview of key SM features and constituent parts is provided.

218

219 1.1 General composition and key parameters

220 In this section I will describe the fields that enter the SM. Their existence and interactions result in
221 the three fundamental forces that are taken into account by the theory. The quanta of these fields are
222 also called fundamental particles and possess a number of properties like mass, charge (or charges),
223 spin etc (see figure 11). The fundamental particles are divided into two groups based on their spin:
224 particles with integer spin are called fermions and those with half-integer spin are bosons.
225 Let's start from the fermion sector. According to the Pauli exclusion principle[7] two fermions can not
226 occupy the same quantum numbers. This in turn, has a consequence that the fermions must occupy

¹There are SM extentions that take into account the non-zero neutrino mass. Then the model gets 7 additional parameters, so their total number reaches 25. Although current thesis only considers the SM where neutrinos are massless.

227 a finite volume in space-time and as a result make up matter. Half of the fundamental fermions
228 have color charge and therefore take part in strong interaction - they are called quarks. The other six
229 fermions do not have color charge and are called leptons (from Greek " $\lambda\epsilon\pi\tau\omega$ " meaning "little", as
230 they are lighter than the quarks of the same generation). Different types of quarks and leptons are also
231 called flavours, so there are 6 flavours of quarks and 6 flavours of leptons.

232 For some reason which is yet unknown the twelve elementary fermions make three generations.
233 Particles in the second and third generations have exactly the same charge and spin as the particles of
234 the first generation, but are heavier and also unstable. Normally the particles of higher generations
235 quickly decay down to their lighter kins of the first generation and can only be observed in cosmic rays
236 and particle accelerators. That means all the matter that surrounds us consists of four fundamental
237 fermions of the first generation²(the first column in Fig. 11).

238 The two quarks of the first generation are called up-quark and down-quark (or u-quark and d-quark
239 for short). All the nuclei of the ordinary matter we see around are built out of these two types of
240 quarks. Quarks are capable of interacting through all three SM forces: electromagnetic, weak and
241 strong. Electrons, muons and tau-leptons are sensitive to electromagnetic and weak interaction, while
242 neutrinos can interact (and therefore be detected) only through weak force. For this reason in particle
243 physics the term "leptons" is sometimes used in a narrow sense referring to electron-like particles only.
244 For all quarks and electron-like particles the antiparticles were observed as well as the corresponding
245 annihilation phenomena. It is still not clear if neutrinos annihilate.

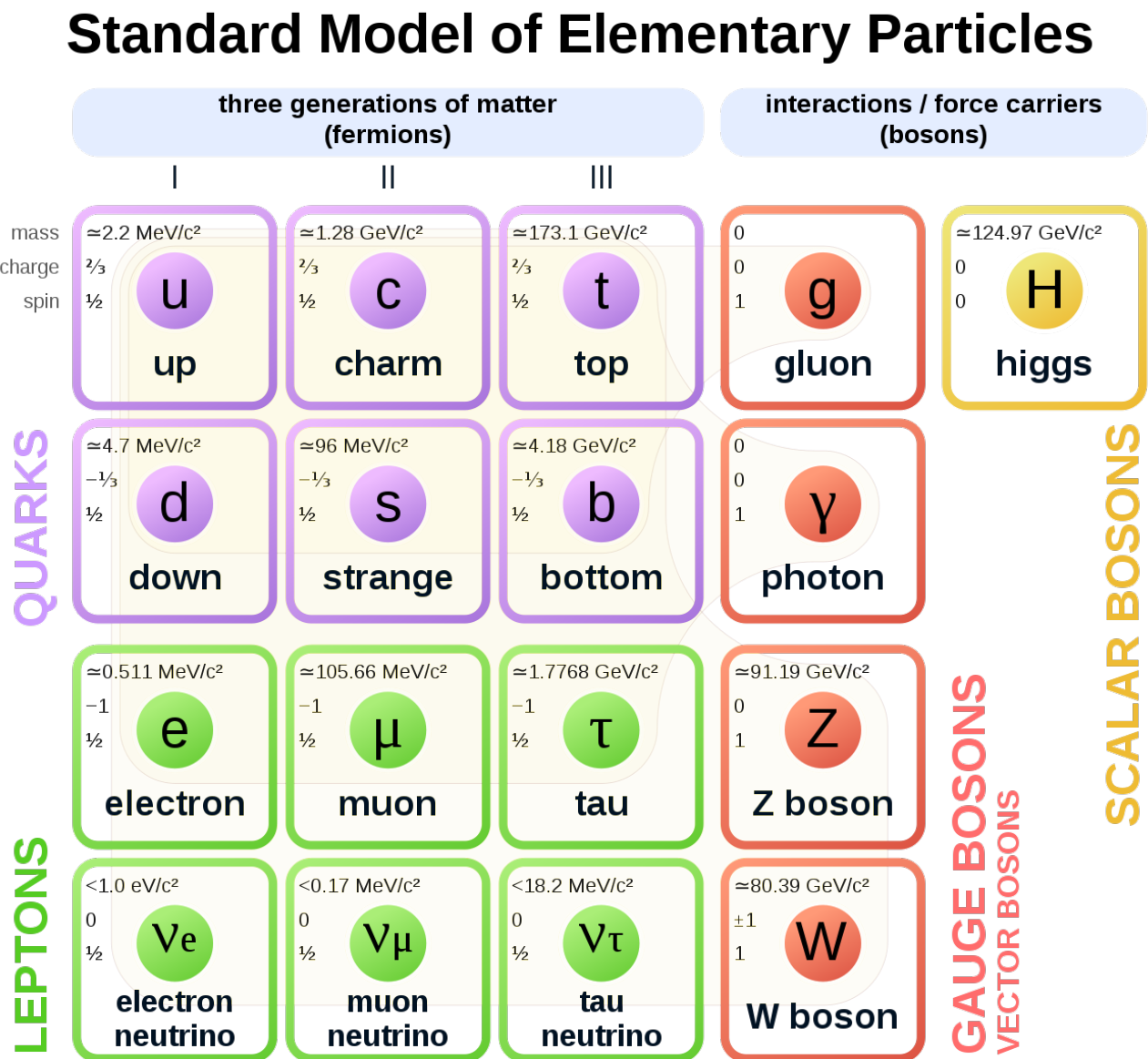
246 From our experience we know that matter interacts with matter. But within the SM fermions do not
247 interact with each other immediately. The interaction is mediated by boson-type particles. The SM
248 includes five types of bosons: four vector bosons serving as force carriers for electromagnetic, weak
249 and strong interactions, and a spinless Higgs boson whose role would be described in more detail in
250 the corresponding subsection 1.4.1. The Higgs boson along with W and Z bosons are massive, while
251 photons and gluons are massless.

252 The masses of the fundamental particles make 12 out of 18 free parameters of the SM³.
253 As it was mentioned, bosons interact with fermions through fundamental interactions. The interaction
254 depends on the charge of the interacting particles and on the type of the interaction itself. Each type
255 interaction has a coupling constant that defines the scale of the interaction. Hence two more parameters
256 to the SM: the strong and electromagnetic coupling constants (the latter is also called the fine structure
257 constant). Weak coupling constant is redundant since it can be obtained from other parameters.
258 And the remaining four parameters are coming from the CabibboKobayashiMaskawa matrix (CKM
259 matrix), that contains information on the strength of the flavour-changing weak interaction. [8].

260 An important feature of the Quantum Field Theory (QFT) is that particles also interact with physical
261 vacuum. For instance, a charged particle polarises the physical vacuum, so the vacuum screens the

²Strictly speaking we already know that this is not completely true for the neutrinos, as they oscillate between the flavours due to their tiny mass. But in the SM neutrinos are assumed massless.

³The masses of W and Z bosons can be replaced by other parameters, e.g. weak mixing angle θ_W and Higgs potential vacuum expectation value (v. e. v.).

**Figure 11:** The list of particles that enters the SM[9].

262 charge of the particle[10].This interaction with virtual particles depends on the energy scale and so
 263 do the observed quantities like charge, mass etc. The SM is able to predict parameter evolution, so
 264 if the value of a certain input parameter q_0 is known at the energy Λ_0 then it is possible to predict
 265 its measurable value q at the energy Λ . This changing of physical parameters is an integral part of
 266 the QFT and is called *renormalisation* [2], [11]. In the picture 12 the dependence of the SM coupling
 267 constants on the energy is shown.

268

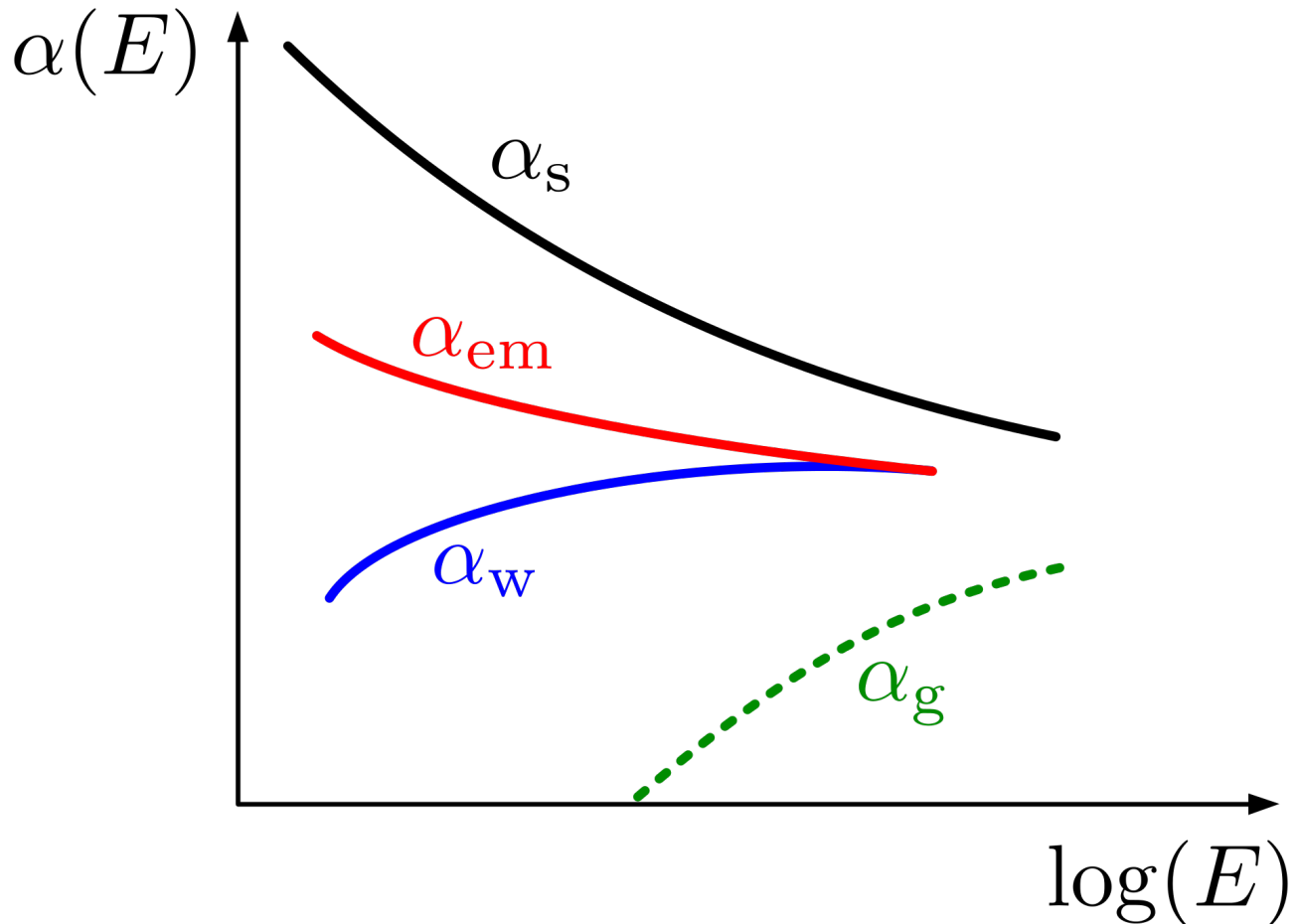


Figure 12: The evolution of the SM running coupling constants [12].

269 As we can see from picture 12 the strong coupling constant is getting smaller with the energy. This
 270 phenomena is called *the asymptotic freedom* [13], [14], [15].

271 **1.2 Classical fields and gauge invariance principle**

272 A consistent mathematical description of fields appears to be more challenging task compared to the
 273 description of physical objects that have definite size and shape. The derivation of Maxwell's equations

274 has been a great success and allowed to obtain the first equations of motion of relativistic fields. It has
 275 also subsequently led to understanding of special relativity [16], [17], [18]. Although for a more general
 276 case of fields other than electromagnetic it would be very useful to adopt a more systematic approach
 277 like that of Lagrangian or Hamiltonian in classical mechanics.

278 It has turned out that for the relativistic case Hamiltonian approach was not quite convenient, as
 279 the dedicated role of time over other degrees of freedom was in discord with relativistic space-time
 280 unification. However it was found possible to describe the fields within the Lagrangian approach. In
 281 the classic mechanics the action of a mechanical system of i mechanical objects is defined as:

$$S = \int L dt = \int \left(\sum_i T_i - U_i \right) dt,$$

282 where T_i and U_i are the kinetic and potential energies of the i^{th} object. Considering that by definition
 283 a field exists in every point of space-time, we need to define the Lagrangian density such that $L =$
 284 $\int \mathcal{L}(\phi, \partial_k \phi, \dot{\phi}) d^3x$, where ϕ is a field and $\partial_k \phi = \nabla \phi$ - the field gradient, $\partial_k = \frac{\partial}{\partial x^k}$, $k = 1, 2, 3$. Here and
 285 further latin indices run through (1, 2, 3) and are used to denote spacial coordinates, while greek
 286 indices denote space-time coordinates and run though (0, 1, 2, 3). So the action would look like:

$$S = \int L dt = \int \mathcal{L}(\phi, \partial_\mu \phi, \dot{\phi}) d^4x, \quad (1.1)$$

287 Now we may use the principle of least action to obtain the equations of motion using the Euler-
 288 Lagrange formalism. Let's check it with the example of electromagnetic fields. The Lagrangian density
 289 of electromagnetic fields in a vacuum can be written like:

$$S = -\frac{1}{4} \int F^{\mu\nu} F_{\mu\nu} d^4x. \quad (1.2)$$

290 Electromagnetic tensor can be defined in terms of electric and magnetic field intensities: $F_{i0} = -F_{0i} = E_i$,
 291 $F_{ij} = \epsilon_{ijk} H_k$, where ϵ_{ijk} - antisymmetric Levi-Civita symbol. Alternatively $F_{\mu\nu}$ can be defined in terms
 292 of 4-potential A_μ :

$$F_{\mu\nu} = \partial_\mu A_\nu - \partial_\nu A_\mu. \quad (1.3)$$

293 Now we can safely apply the variational principle and putting $\delta S = 0$ obtain the Maxwell equations in
 294 a vacuum:

$$\partial_\mu F_{\mu\nu} = 0. \quad (1.4)$$

295 Noticing the symmetries of the system and using the Noether's theorem[19] we can find the invariants
 296 of electromagnetic field. For example, translational symmetry in time and space ensures conservation
 297 of energy and momentum. Let's now consider a symmetry of a different kind. The field potential can be
 298 shifted by a gradient of an arbitrary function $\alpha = \alpha(x^\mu)$:

$$\begin{aligned} A_\mu(x) &\rightarrow A'_\mu(x) = A_\mu(x) + \partial_\mu \alpha(x) \\ F_{\mu\nu} &\rightarrow F'_{\mu\nu} = \partial_\mu(A_\nu(x) + \partial_\nu \alpha(x)) = \partial_\mu A_\nu - \partial_\nu A_\mu = F_{\mu\nu}. \end{aligned} \quad (1.5)$$

299 Let's now consider the electromagnetic theory in the presence of charges and currents:

$$\mathcal{L} = -\frac{1}{4}F^{\mu\nu}F_{\mu\nu} + j^\mu A_\mu. \quad (1.6)$$

300 Now we have an interaction of a field potential A_μ with 4-current $j^\mu = (-\rho, j^i)$. It turns out to be a
301 general property of the field theories: the only form of interaction allowed is between a gauge field and
302 a current. After applying the gradient field transformation and the least action principle we can obtain
303 the corresponding conservation law:

$$\partial_\mu j^\mu = 0. \quad (1.7)$$

304 So this gradient symmetry[2] or as it is called more often gauge symmetry leads to the conservation of
305 electric current. If a theory is invariant under gauge transformations then it is called a gauge invariant
306 theory. As we have just seen electrodynamics is the simplest example of such a theory. Taking gauge
307 symmetries into consideration [20] has played a huge role in the development of the SM.

308 Gauge degree of freedom can be constrained in arbitrary way by applying additional conditions on the
309 gauge function. This is called fixing the gauge and becomes necessary after quantization. Any physical
310 result must be gauge-invariant, i.e. must not depend on the gauge.

311 1.3 Quantum electrodynamics

312 Quantum Electrodynamics (QED) is a theory of interaction between light and electrically charged
313 particles. Historically it was the first quantum field theory to reach good agreement between quantum
314 mechanics and special relativity. QED vacuum has zero expectation value. Nowadays it is considered
315 to be one of the most precise physical theories ever: theory predictions and experiment results agree up
316 to $O(10^{-8})$. It has also served as a model for composition of the subsequent parts of the SM, describing
317 other fundamental interactions.

318 Let's consider free Dirac field based Lagrangian:

$$\mathcal{L} = \bar{\psi}(x)(i\cancel{\partial} + m)\psi(x), \quad (1.8)$$

319 where ψ and $\bar{\psi}$ are Dirac wave function and its complex conjugate respectively, $\cancel{\partial} \equiv \gamma_\mu \partial^\mu$, γ_μ is one of
320 the four gamma-matrices and m is the mass of the Dirac field. Such a theory, though, would not be
321 physically consistent. This reflects the fact the quantum nature of spin and spinor fields have to be
322 treated as quantum fields. For instance, an attempt to calculate the energy of a Dirac field would lead
323 to a contradiction: the energy would not be positively defined, as some spinors would have negative
324 energies.

325 This Lagrangian has an internal symmetry to the U(1) transformation: $\psi \rightarrow e^{-i\alpha(x)}\psi$, $\bar{\psi} \rightarrow e^{i\alpha(x)}\bar{\psi}$.
326 According to Noether's theorem this symmetry implies current conservation: $j^\mu = \bar{\psi}\gamma^\mu\psi$. Now let's get
327 the combined Lagrangian of electromagnetic and Dirac fields, adding the interaction term:

$$\mathcal{L} = \mathcal{L}_{Dirac^{free}} + \mathcal{L}_{EM^{free}} + \mathcal{L}_{Interaction} = -\frac{1}{4}F^{\mu\nu}F_{\mu\nu} + \bar{\psi}(x)(i\cancel{\partial} + m)\psi(x) - q\bar{\psi}\gamma^\mu A_\mu\psi, \quad (1.9)$$

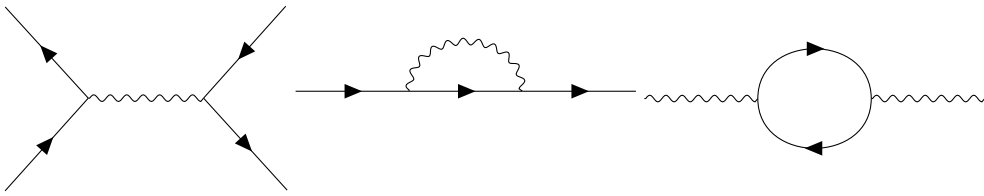


Figure 13: The QEQ diagrams: Compton scattering, electron self-energy, photon self-energy.

328 where q represents the elementary electric charge. This Lagrangian above is gauge invariant and can be
329 rewritten in a more convenient form:

$$\mathcal{L} = -\frac{1}{4}F^{\mu\nu}F_{\mu\nu} + \bar{\psi}(x)(iD + m)\psi(x), \quad (1.10)$$

330 where $D_\mu = \partial_\mu + iqA_\mu$ is a covariant derivative. If one considers space-time in the presence of a field as
331 curved, then A_μ would play a role of connectivity. It must be noted that values like m and q meaning
332 electron mass and charge⁴ are the SM input parameters mentioned in 1.1.

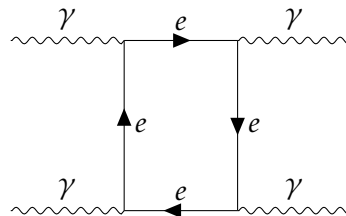
333 Further calculations are to be performed by the means of the quantum field theory formalism that
334 treats interaction terms like a perturbation to the free fields, making power series expansion in the
335 coupling constant. In the case of electrodynamics the coupling constant is quite small so good precision
336 is reached soon. Since the photons do not directly interact with other photons, QED allows only one
337 type of vertex - with two electron lines and one photon line.

338

339 Although the tree-level processes and diagrams were well understood by 1930th, the loop diagrams
340 were properly explained only by the end of the 1940th making it possible obtain numerical results
341 of the higher orders of power series expansion and achieve higher precision predictions for QED
342 processes[21], [10], [22], [23], [24], [25], [26], [27].

343 It must be noted that although direct photon-photon interaction is impossible, light-by-light scattering
344 is still possible through loops:

345



346

347 This process was theoretically described in 1936 [28] and experimentally observed 83 years after in
348 heavy ion collisions at the LHC [29].

⁴Charge of the electron is related to the electromagnetic coupling constant.

349 1.4 Electroweak theory and the Higgs mechanism

350 All the fermions of the standard model are subject to weak interaction, so its importance for physical
 351 processes can not be underestimated. At low energy weak interaction manifests itself mainly through
 352 flavour-changing decays like beta-decay and muon decay. The electroweak theory was created in the
 353 end of 1950s[11] [5] [30] thanks to numerous experimental results that allowed to shape its properties.
 354 The theory assumed that the electromagnetic and weak fundamental forces are actually manifestation
 355 of the same field that has a gauge symmetry $SU(2)_L \times U(1)$ with massive charged and neutral bosons.
 356 A few years later the structure of electroweak vacuum was explained along with the mechanism that
 357 has allowed the bosons to gain mass [31], [32]. Assuming this the Lagrangian of the electroweak theory
 358 must consist of three parts[33]:

- 359 • Gauge fields that would mediate the interaction.
- 360 • Fermions that interact with gauge fields
- 361 • A scalar Higgs field with non-zero vacuum energy that breaks the $SU(2)$ symmetry and couples
 362 to the fermions.

$$\mathcal{L}_{EW} = \mathcal{L}_{Gauge} + \mathcal{L}_{Higgs} + \mathcal{L}_{Fermions} \quad (1.11)$$

363 1.4.1 Electroweak gauge fields

364 As it was already pointed out before, knowing the symmetries of a physical system allows one to
 365 compose the gauge fields Lagrangian. The part with $U(1)$ symmetry would look like the electromagnetic
 366 field from 1.2 having the hypercharge Y , a vector potential B_μ and a gauge coupling g_1 . The $SU(2)$ field
 367 would have 3 vector components $W_\mu^{1,2,3}$, three isospin operators I_1, I_2, I_3 and a gauge coupling g_2 . We
 368 can pick the Pauli matrices σ^i as the representation of generators of the $SU(2)$ group, then the structure
 369 constants are ϵ_{abc} - Levi-Civita symbol.

$$\begin{aligned} \mathcal{L}_G &= -\frac{1}{4}B_{\mu\nu}B^{\mu\nu} - \frac{1}{4}W_{\mu\nu}^a W^{\mu\nu,a}B_{\mu\nu} = \partial_\mu B_\nu - \partial_\nu B_\mu \\ W_{\mu\nu}^a &= \partial_\mu W_\nu - \partial_\nu W_\mu + g_2 \epsilon_{abc} W_\mu^b W_\nu^c, \end{aligned} \quad (1.12)$$

370 where the term $g_2 \epsilon_{abc} W_\mu^b W_\nu^c$ appears due to the non-Abelian nature of the $SU(2)$ group (the generators
 371 don't commute).

372 1.4.2 Fermion sector

373 Each fundamental fermion generation expressed as left-handed doublets and right-handed singlets is a
 374 fundamental representation of the group $SU(2) \times U(1)$:

$$\begin{pmatrix} \nu_e \\ e \end{pmatrix}_L, \begin{pmatrix} \nu_\mu \\ \mu \end{pmatrix}_L, \begin{pmatrix} \nu_\tau \\ \tau \end{pmatrix}_L, (e_R), (\mu_R), (\tau_R), \quad (1.13)$$

$$\begin{pmatrix} u \\ d \end{pmatrix}_L, \begin{pmatrix} c \\ s \end{pmatrix}_L, \begin{pmatrix} b \\ t \end{pmatrix}_L, (u_R), (d_R), (c_R), (s_R), (t_R), (b_R). \quad (1.14)$$

375 Their quantum states are classified using the following quantum numbers: weak isospin I_3, I , weak
376 hypercharge Y . Their electric charge can be obtained using the Gell-Mann-Nishijima relation:

$$Q = I_3 + \frac{Y}{2}. \quad (1.15)$$

377 The fermions are divided by their chirality: only the left-handed particles take part in weak
378 interaction. The left-handed fermion fields of each lepton and quark generation j

$$\psi_j^L = \begin{pmatrix} \psi_{j+}^L \\ \psi_{j-}^L \end{pmatrix} \quad (1.16)$$

379 make SU(2) doublets, with indices $\sigma = \pm$, while the right-handed fermions can be written as singlets:

$$\psi_j^R = \psi_{j\sigma}^L. \quad (1.17)$$

380 Like in the electromagnetic case we can define the covariant derivative that would ensure the gauge
381 invariance of the Lagrangian:

$$D_\mu = \partial_\mu - ig_2 I_a W_\mu^a + ig_1 \frac{Y}{2} B_\mu, \quad (1.18)$$

382 with $I_a \equiv \frac{\sigma_a}{2}$, then fermion Lagrangian takes the following form:

$$\mathcal{L}_{Fermions} = \sum_f \bar{\psi}_j^L i \gamma^\mu D_\mu \psi_j^L + \sum_{f,\sigma} \bar{\psi}_{f,\sigma}^R i \gamma^\mu D_\mu \psi_{f,\sigma}^R. \quad (1.19)$$

383 1.4.3 Higgs fields breaking the symmetry

384 The Higgs field is represented by single complex scalar doublet field $\Phi(x)$, that has 4 independent
385 components. It spontaneously breaks the $SU(2) \times U(1)$ gauge symmetry, leaving the $U(1)_{EM}$ symmetry
386 intact. The Higgs field doublet has the hypercharge $Y = 1$:

$$\Phi(x) = \begin{pmatrix} \phi^+(x) \\ \phi^0(x) \end{pmatrix}. \quad (1.20)$$

387 The Higgs field Lagrangian with non-zero vacuum expectation value:

$$\mathcal{L}_{Higgs} = (D_\mu \Phi)^+ (D_\mu \Phi) - V(\Phi) + \mathcal{L}_{Yukawa}. \quad (1.21)$$

388 The gauge invariance of the Higgs Lagrangian is ensured in the traditional way by using the covariant
389 derivative:

$$D_\mu = \partial_\mu - ig_2 I_a W_\mu^a + i\frac{g_1}{2} B_\mu. \quad (1.22)$$

390 Higgs potential contains the mass term and quartic self-interaction:

$$V(\Phi) = -\mu^2 \Phi^+ \Phi + \frac{\lambda}{4} \partial_\mu (\Phi^+ \Phi)^2. \quad (1.23)$$

391 Valuum expectetion value $\langle \Phi \rangle$ does not vanish:

$$\langle \Phi(x) \rangle = \frac{1}{\sqrt(2)} \begin{pmatrix} 0 \\ v \end{pmatrix}, \quad v = \frac{2\mu}{\sqrt(\lambda)}. \quad (1.24)$$

392 Applying the unitarity gauge [34] we can constraint three out of four degrees of freedom of the Higgs
393 field and rewrite the Higgs doublet in the following way:

$$\Phi(x) = \frac{1}{2} \begin{pmatrix} 0 \\ v + H(x) \end{pmatrix}, \quad (1.25)$$

394 which leaves us with a physical real neutral scalar field $H(x)$ with

$$M_H = \sqrt(2)\mu. \quad (1.26)$$

395 This real field would couple to itself forming triple and quartic self-coupling vertices, to the gauge
396 fields through the covariant derivatives and to the charged fermions, giving them mass. Yukawa term
397 in Lagrangian the unitary gauge:

$$\mathcal{L}_{Yukawa} = - \sum_f m_f \bar{\psi}_f \psi_f - \sum_f \frac{m_f}{v} \bar{\psi}_f \psi_f H, \quad (1.27)$$

398 where

$$m_f = g_f \frac{v}{\sqrt(2)} = \sqrt(2) \frac{g_f}{g_2} M_W. \quad (1.28)$$

399 Higgs coupling constants to the corresponting fermion flavour are denoted as g_f . This relation
400 between the Higgs coupling and the mass of the W boson illustrates how much the SM parameters are
401 intertwined and particularly underlines the importance of the M_W measurement.

402 1.4.4 Physical interpretation of gauge fields and parameters

403 Higgs coupling to the gauge fields results in the following terms in the Lagrangian:

$$\frac{1}{2} \frac{g_2}{2} v (W_1^2 + W_2^2) + \frac{v^2}{4} (W_\mu^3, B_\mu) \begin{pmatrix} g_2^2 & g_1 g_2 \\ g_1 g_2 & g_1^2 \end{pmatrix} \begin{pmatrix} W_\mu^3 \\ B_\mu \end{pmatrix}. \quad (1.29)$$

404 In order to get the physical meaning of this expression let us make a transition to the basis of physical
405 fields:

$$\begin{aligned} W_\mu^\pm &= \frac{1}{\sqrt{2}}(W_\mu^+ \mp iW_\mu^-) \\ \begin{pmatrix} Z_\mu \\ A_\mu \end{pmatrix} &= \begin{pmatrix} \cos\theta_W & \sin\theta_W \\ -\sin\theta_W & \cos\theta_W \end{pmatrix} \begin{pmatrix} W_\mu^3 \\ B_\mu \end{pmatrix}, \end{aligned} \quad (1.30)$$

406 where θ_W is called the weak mixing angle or the Weinberg angle. In the new basis expression 1.29 has
407 transparent physical sense:

$$M_W^2 W_\mu^+ W^{-\mu} + \frac{1}{2}(A_\mu, Z_\mu) \begin{pmatrix} 0 & 0 \\ 0 & M_Z^2 \end{pmatrix} \begin{pmatrix} A_\mu \\ Z_\mu \end{pmatrix}, \quad (1.31)$$

408 with

$$\begin{aligned} M_W &= \frac{1}{2}g_2 v \\ M_Z &= \frac{1}{2}\sqrt{g_1^2 + g_2^2}v. \end{aligned} \quad (1.32)$$

409 The mixing angle θ_W also has a very clear physical meaning:

$$\cos\theta_W = \frac{g_2}{g_1^2 + g_2^2} = \frac{M_W}{M_Z}. \quad (1.33)$$

410 With A_μ having a sense of electromagnetic potential its coupling to the electron must have a physical
411 meaning of the electric charge $e = \sqrt{4\pi\alpha}$ we can express e in terms of gauge couplings:

$$e = \frac{g_1 g_2}{g_1^2 + g_2^2}, \quad g_2 = \frac{e}{\sin\theta_W}, \quad g_1 = \frac{e}{\cos\theta_W}. \quad (1.34)$$

412 Thus the demonstrated Weinberg rotation fully replaces the original parameters $g_1, g_2, \lambda, \mu^2, g_f$ by
413 another set of measurable values e, M_W, M_Z, M_H, m_f which are the input parameters of the SM.

414 1.5 Chromodynamics

415 The Quantum Chromodynamics (QCD) is a non-Abelian gauge theory that describes strong interaction.
416 The QCD is symmetric under unbroken SU(3) color symmetry, so the interaction scheme is built in the
417 same way as electromagnetic and electroweak theories. To preserve the gauge invariance the gauge
418 field of gluons is introduced with 8 components, since SU(N) group has $\frac{N^2-1}{2}$ independent elements.
419 The gluons are massless vector bosons like the photons, although because of the non-Abelian nature of
420 the gauge group they couple not only to the fermions but also to the other gluons. The gauge invariant
421 QCD Lagrangian with kinetic term containing covariant derivative would look like:

$$\begin{aligned} \mathcal{L}_{QCD} &= -\frac{1}{4}F_{\mu\nu}^a F_a^{\mu\nu} + \bar{\psi}_a(i(\gamma^\mu D_\mu)^{ab} - m\delta^{ab})\psi_b, \\ F_{\mu\nu}^a &= \partial_\mu A_\nu^a - \partial_\nu A_\mu^a + g_s f^{abc} A_\mu^b A_\nu^c, \\ D_\mu &= \partial_\mu + ig_s A_\mu^a t_a. \end{aligned} \quad (1.35)$$

422 with ψ being the quark field, m is the mass of the quark, $a, b = 1, 2, \dots, 8$ are the color indices, g_s is the
423 strong coupling constant, f^{abc} are the structure constants of the SU(3) group and t_a are the generators

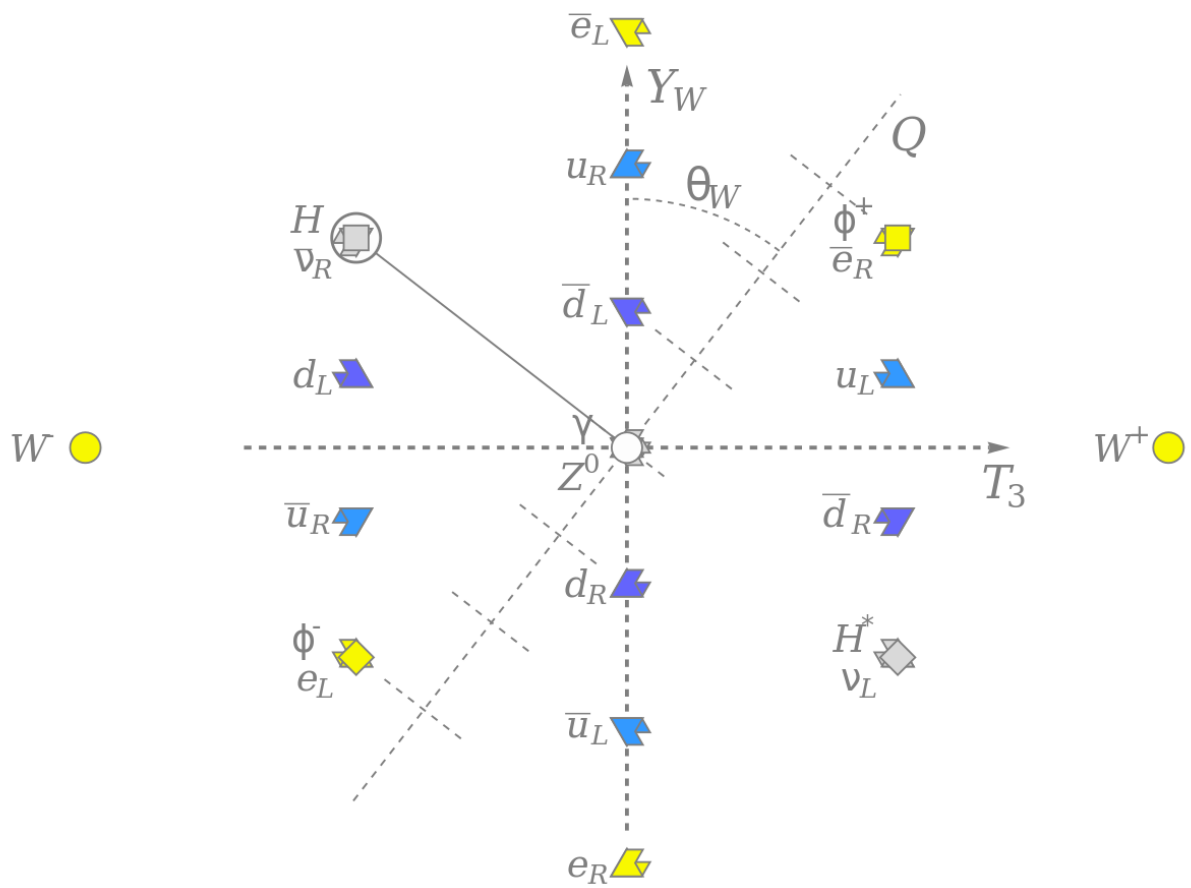


Figure 14: Electroweak sector and the Weinberg rotation [12].

424 of the SU(3) group.

425 As it was already mentioned in 1.3 quantitative calculations in QFT treat particle interaction as a
 426 perturbation to the free field theory. Coupling constant is considered to be a small parameter so every
 427 next power of the coupling constant is much smaller than the previous. Thanks to the asymptotic
 428 freedom α_s becomes small at higher energies and allows perturbative calculations. But at certain energy
 429 scale called $\Lambda_{QCD} \approx 200$ MeV, QCD becomes non-perturbative. It means we may no longer assume that
 430 interaction is a small perturbation of the free fields. This phenomena is known as the *color confinement*.
 431 Because of the color confinement we can only observe colorless objects like baryons and mesons, but not
 432 quarks and gluons. If a high-energetic parton gets torn out of a hadron then it creates an avalanche-like
 433 process creating quark-antiquark pairs until fully hadronizes (see pic. 15) confining its color. Such an
 434 avalanche is called a hadronic jet.

435

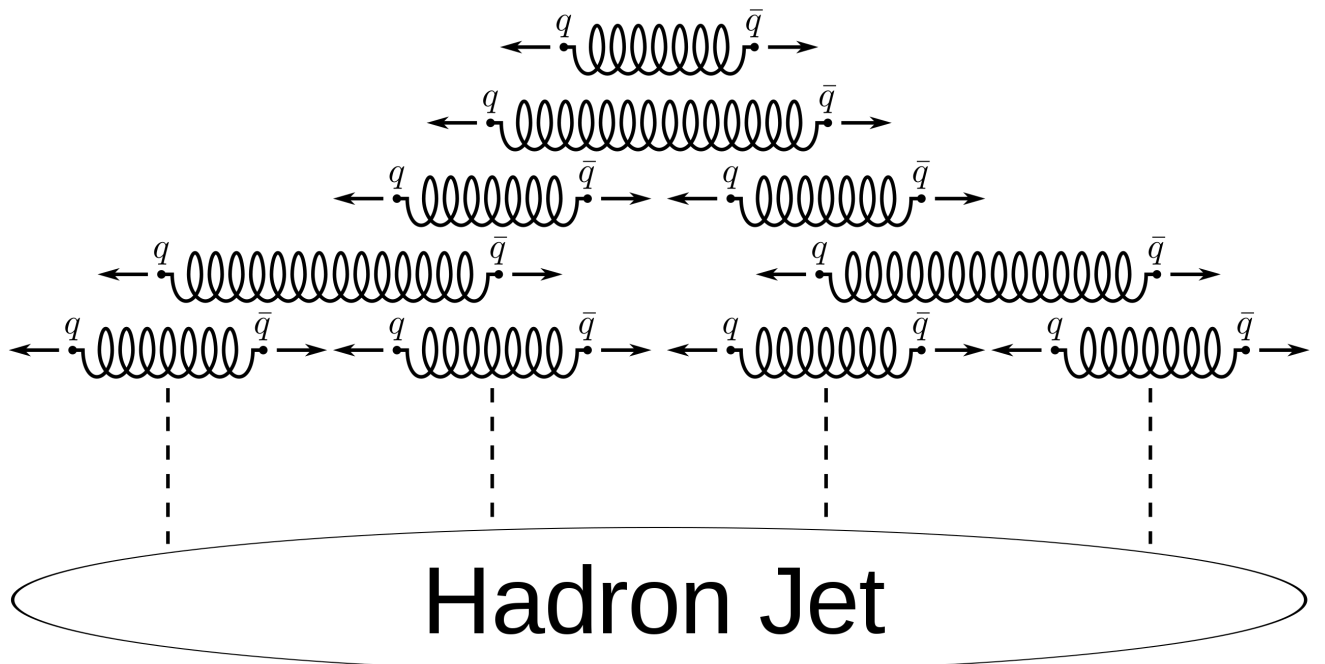


Figure 15: The formation of a jet [35].

436 Currently there is no viable physical theory that would describe QCD vacuum and low-energy
 437 behaviour of quarks and gluons. This also means that although nuclear forces are evidently residuals
 438 of the QCD interaction of partons within the baryons, there is no continuity between the QCD and
 439 nuclear physics. Confinement and low-energy QCD remain to be an unsolved problem of modern
 440 physics.

441

442

2 The W boson

443 *"Potentielle citation sans aucun rapport avec le sujet"*

444 — Personne inconnue, *contexte à déterminer*

445 **2.1 Introduction**

446 **2.2 W boson production at the LHC**

447 **2.3 W boson decay**

448 **2.4 W boson detection**

449 **2.5 Precision measurements of WpT**

450 **2.6 Precision measurements of W mass**

3

The Large Hadron Collider

451

452

453 *"Potentielle citation sans aucun rapport avec le sujet"*

454 — Personne inconnue, contexte à déterminer

455 3.1 Introduction

456 The study of elementary particles naturally demands a stable source of particles. At the dawn of
457 particle physics the two main sources were radioactive materials and the cosmic rays. However soon
458 researchers became in need of a more reliable source of particles in terms of particle energy, luminosity
459 and experimental repeatability. This has commenced the era of particle accelerators.

460 The first examples of particle accelerators were designed in late 1920s and early 1930s. Two different
461 designs emerged: linear and circular. The former accelerates particles via electric field during the
462 single pass through the machine, while the latter uses magnetic field to make accelerated particles go
463 in circles allowing to re-accelerate the same beam many times. On the other hand the circular design
464 comprises energy losses due to Bremsstrahlung radiation.

465 In the second half of the XX century the accelerators gradually got bigger and bigger in both size and
466 center-of-mass energy of the accelerated particles. This has allowed to create an experimental basis for
467 the development of modern particle physics, notably the Standard Model.

468 Up to this day the biggest particle accelerator with the highest center-of-mass energy is the Large
469 Hadron Collider (LHC). LHC is a circular collider that lies in a tunnel of 27 km under the French-Swiss
470 border next to Geneva [Bruening]. In 2012 two biggest experiments of LHC have claimed the discovery
471 of the Higgs boson, the last elementary particle predicted by the Standard Model which was not yet
472 discovered by that time. [1], [2].

473 3.2 The LHC running sequence

474 It takes quite a journey for a proton to travel from a hydrogen tank (Fig. 31) into one of the LHC's
475 collision points. A resourceful system of pre-accelerators is necessary to make the proton beam ready
476 to get injected into one of the two LHC beam pipes. The LHC accelerator complex was not built from
477 scratch - it uses vast CERN infrastructure, that was built for the previous particle physics experiments.
478 After stripping the electrons off the atoms of hydrogen using the magnetic field the yielded protons get



Figure 31: ATLAS A hydrogen tank supplies LHC with protons [3].

479 accelerated to the energy of 50 MeV by Linac 2¹ [4]. After that the beam gets into Proton Synchrotron
 480 Booster (PSB) to be accelerated to 1.4 GeV. The next link of the pre-acceleration chain is the Proton
 481 Synchrotron (PS) - a true veteran among CERN accelerators that first accelerated protons in 1959
 482 holding the world record in acceleration energy. Currently thanks to PSB and other modifications it
 483 can sustain proton beam intensity 1000 times larger than back in 1959. The PS accelerates the beam
 484 up to 25 GeV and conveys it further to the Super Proton Synchrotron (SPS) - the second-largest particle
 485 accelerator at CERN. Back in 1983 the massive electroweak bosons were discovered at the SPS but even
 486 now it serves as a main accelerator for a NA61/SHINE, NA62 and COMPASS experiments. The SPS
 487 raises the beam energy to 450 GeV and finally injects it into the LHC beam pipes (see Fig 32).
 488

489 The LHC has inherited its 27 km tunnel from the predecessor, an electron-positron collider called
 490 Large Electron-Positron (LEP). However, all the LEP hardware has been replaced to sustain the
 491 conditions of the LHC beam. About 2/3 of the LHC circumference length is occupied by the dipole
 492 magnets that bend the trajectory of the proton beam to keep it within the pipe. These magnets use
 493 superconducting coils that conduct a current of 11080 amperes to produce a magnetic field of 8.3 tesla
 494 Proton acceleration is maintained by the radiofrequency (RF) cavities (Fig. 33a). Besides acceleration
 495 particles the RF cavities are also responsible for beam bunching i.e. separating the beam into a train of
 496 separated particle packs, each containing about 10^{11} protons. During LHC Run 2 the bunches were
 497 separated by 7 meters (25 ns) with a maximum of 2556 circulating bunches. The LHC has four crossing
 498 points, where the two beams are crossed in order to collide protons. Naturally, the particle detectors
 499 are installed at these four points. Before getting directed at the crossing point the beams get squeezed to
 500 make their cross-section as small as $16 \mu\text{m}^2$ (Fig 34a).

¹After Run 2 Linac 2 has been decommissioned to be succeeded by Linac 4.

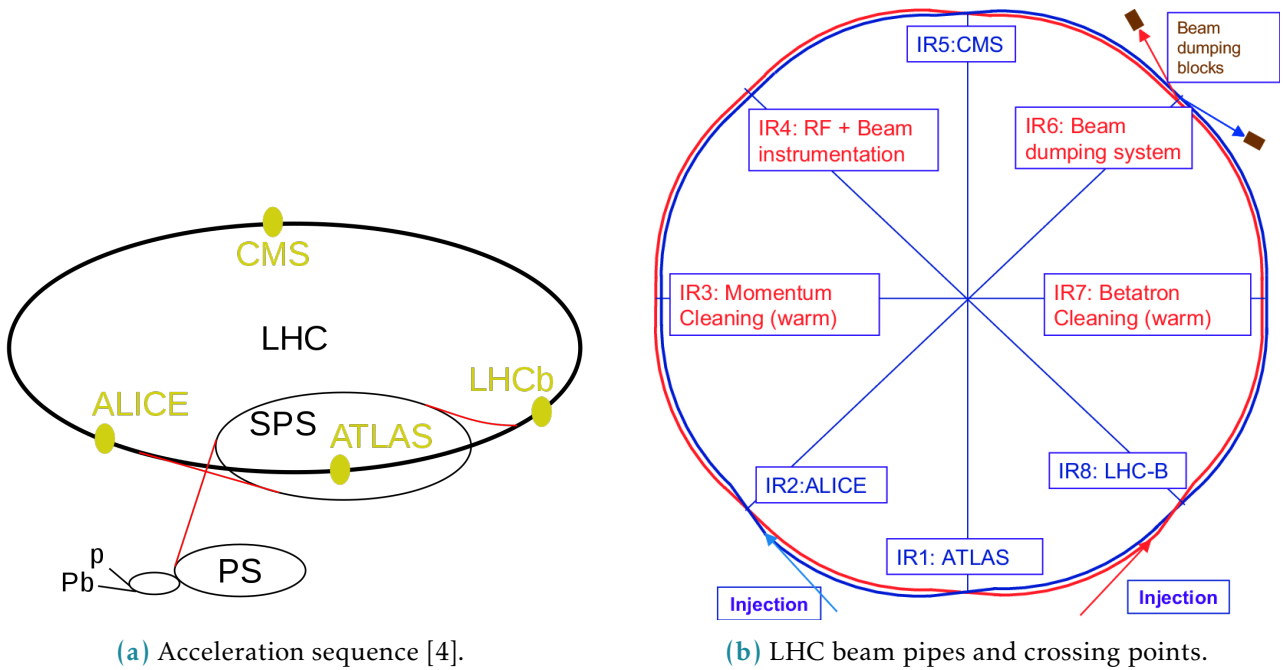


Figure 32: Schematic depiction of the LHC ring.

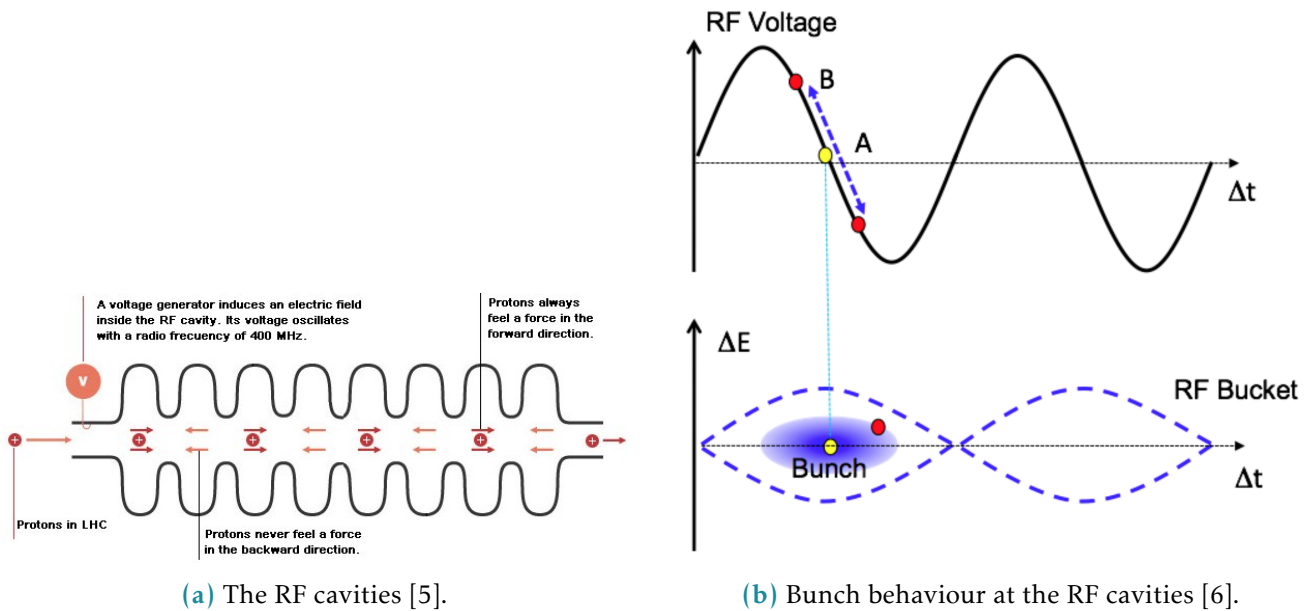
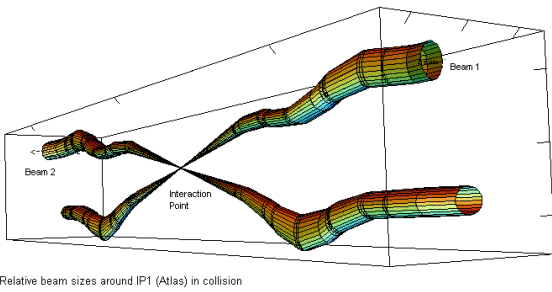
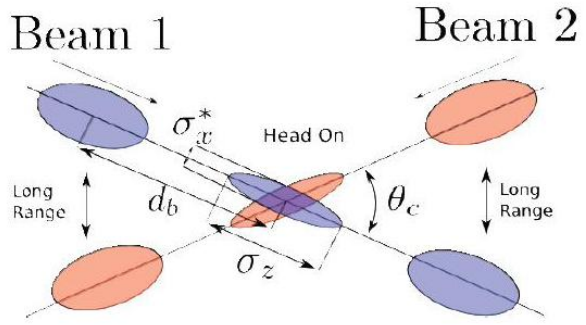


Figure 33: Bunching at RF cavities



(a) The two beams getting squeezed at the IP [7].



(b) Bunches at the collision point [8].

Figure 34: The crossing

501 In order to estimate the number of single proton-proton interactions in the crossing beams a value
 502 called instantaneous luminosity (simply called luminosity) is introduced. It is the proportionality factor
 503 between the number of events per second dR/dt and the cross-section σ_p :

$$\frac{dR}{dt} = \mathcal{L} \cdot \sigma_p.$$

504 For the case of head-on collisions the luminosity would equal to [9]:

$$\mathcal{L} = \frac{N_1 N_2 f N_b}{4\pi \sigma_x \sigma_y}, \quad (3.1)$$

505 with N_1 and N_2 being the intensities of the two colliding beams, f is the revolution frequency, N_b -
 506 number of bunches per beam, σ_x, σ_y - r.m.s. beam widths in the corresponding dimensions, assuming
 507 that the bunches in both beams have the same size and Gaussian profiles.
 508

509 Head-on crossing of the beams would ensure maximal luminosity given the same beams, but on the
 510 other hand the measurement would suffer from unwanted beam-to-beam effects. To avoid it the beams
 511 at the LHC are crossed at an angle, which is called the crossing angle 34b. For the case of head-on
 512 collisions the luminosity gets a factor \mathcal{F} [9]:

$$\mathcal{L} = \frac{N_1 N_2 f N_b}{4\pi \sigma_x \sigma_y} \cdot \mathcal{F}, \quad (3.2)$$

513 with geometric factor

$$\mathcal{F} = \frac{1}{\sqrt{1 + \left(\frac{\sigma_s}{\sigma_x} \frac{\theta_c}{2}\right)}},$$

514 where σ_s is the r.m.s. of the bunch length and θ_c is the crossing angle. Varying the parameters like
 515 beam intensity, bunch spacing, beam profile, crossing angle and others becomes a flexible tool for
 516 luminosity control. This comes in handy for different physics analysis, as some processes are rare
 517 and demand as much luminosity as possible (this is true, for example, for most of the Higgs studies),

Collision energy	Year	Integrated luminosity, pb^{-1}	Total uncertainty, %
5 TeV	2017	258	1.6
13 TeV	2017	148	2.1
13 TeV	2018	193	1.5

518 whereas the others suffer from high pile-up conditions. Instantaneous luminosity integrated over a
 519 period of time is called the integrated luminosity:

$$\mathcal{L}_{int} = \int_0^T \mathcal{L}(t) dt, \quad (3.3)$$

520 and is directly related to the number of observed events $\mathcal{L}_{\text{int}} \cdot \sigma_p = N_{events}$. Precise measurement of the
 521 integrated luminosity is crucial for the LHC results and serves as one of the nuisance parameters for
 522 most of the analyses. A comprehensive overview on the luminosity determination at proton colliders
 523 can be found here [10]. Absolute luminosity measurements at the LHC are performed predominantly
 524 using the van-der-Meer (vdM) scan method [11], [12].

525 3.3 Special low pile-up run durin LHC Run 2

526 During the Run 2 that lasted from 2015 to 2018 the ATLAS experiment has collected $146.9 fb^{-1}$ of data
 527 under different bunch crossing conditions. However the precise measurement of the W boson-related
 528 processes demands special conditions. High number of proton-proton collisions per bunch crossing
 529 leads to contamination of the final state signal with soft collisions products. This effect, known as
 530 pile-up, complicates object reconstruction and results in systematic uncertainties growth. For this
 531 reason two special runs with low number of interactions per bunch crossing have been performed by
 532 the LHC in 2017 and 2018 at he energies of 5 and 13 TeV.

533 The table ?? contains information on the data collected at ATLAS experiment during the special low
 534 pile-up run with $\langle \mu \rangle \approx 2$.

535

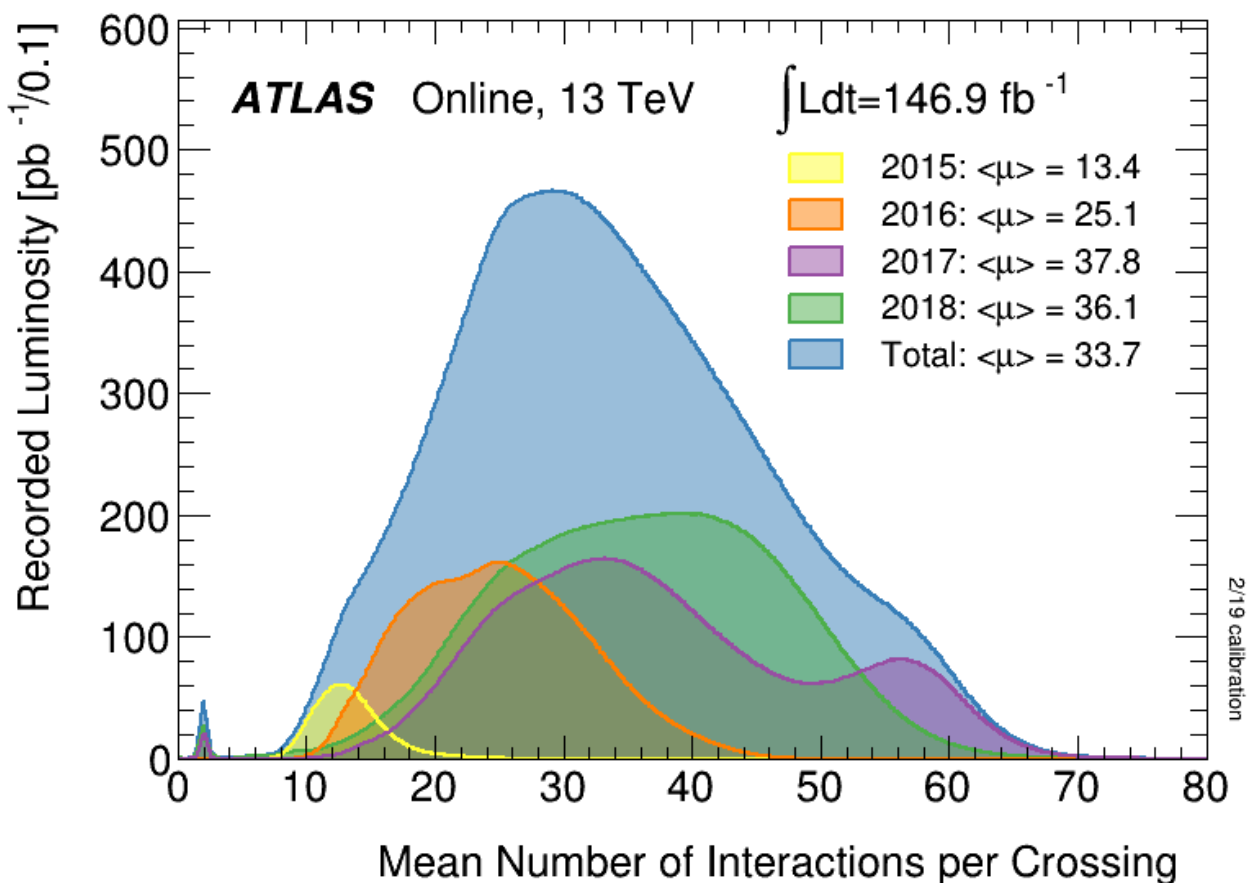


Figure 35: Number of Interactions per bunch crossing in ATLAS Run 2 [13]. A little bump around $\mu \approx 2$ corresponds to special low pile-up runs.

The ATLAS detector

538 “Potentielle citation sans aucun rapport avec le sujet”

— Personne inconnue, contexte à déterminer

540 4.1 General description and layout

ATLAS experiment is a multipurpose detector at the LHC built, along with its peer Compact Muon Solenoid (CMS), in order to probe the p-p, A-A and p-A collisions using the full LHC luminosity [1]. Being the largest (but not the heaviest) detector ever built for a collider experiment the ATLAS detector comprises 44m in length, 25m in height and weights 7000 tonnes.

545 The detector has a cylindrical shape and is an onion-like arrangement of several detector systems
546 centered at the Interaction Point (IP) as shown in fig. 41. The sub-detectors operate in the magnetic
547 field created by the solenoid and toroid magnets (ATLAS owes its name to the latter). Data acquisition
548 and recording is controlled by the Trigger and Data Acquisition (TDAQ) systems, allowing eventually
549 to lower the event rate to a value, acceptable for the data storage [2]. The named systems are described
550 in more detail in this chapter.

551 4.2 Coordinate system

The ATLAS results often reference ATLAS coordinates briefly described in this subsection. The origin of the right-handed coordinate system is placed at the IP with z -axis directed along the beam direction. This, in turn, defines the transverse x - y plane with x axis pointing towards the center of the LHC ring and y axis directed upwards. All transverse observables like p_T and E_T are defined in this 2D plane. Besides the mentioned Cartesian coordinates the azimuthal angle ϕ is defined in the transverse plane around the beam axis. Polar angle θ is the elevation angle measured from the beam axis. The following metric quantities are also to be mentioned:

- Pseudorapidity $\eta = -\ln \tan(\theta/2)$,
 - Rapidity $y = 1/2 \ln [(E+p_z)/(E-p_z)]$
 - The distance between particles $\Delta R = \sqrt{\Delta\eta^2 + \Delta\phi^2}$

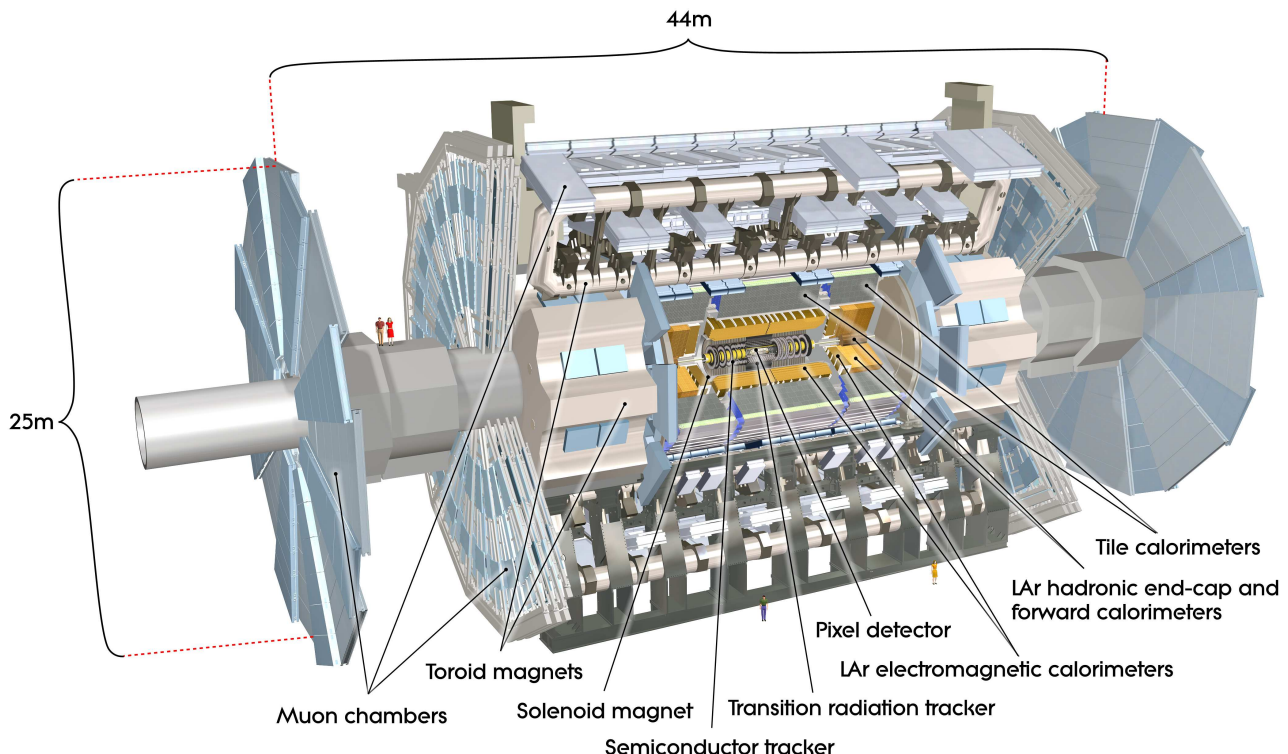


Figure 41: ATLAS detector general layout

562 4.3 Magnet system and magnetic field

563 ATLAS has a hybrid system of four superconducting magnets which has 22 m in diameter, 26 m in
 564 length and stores an energy of 1.6 GJ [3]. The windings of the magnets are schematically shown in fig.
 565 42. The four magnets that comprise the magnet system are the following:

- 566 • The central solenoid is aligned with the beam axis providing 2T axial magnetic field for the inner
 567 detector.
- 568 • A barrel toroid produces toroidal magnetic field of about 0.5T for the muon detectors in the
 569 barrel region.
- 570 • Two end-cap toroids produce toroidal magnetic field of approximately 1T for the muon detectors
 571 in the end-cap regions.

572 4.4 Inner detector

573 The ATLAS Inner Detector (ID) is designed to deliver pattern recognition, high-resolution momentum
 574 measurement [4],[5] along with primary and secondary vertex determination for charged particle tracks

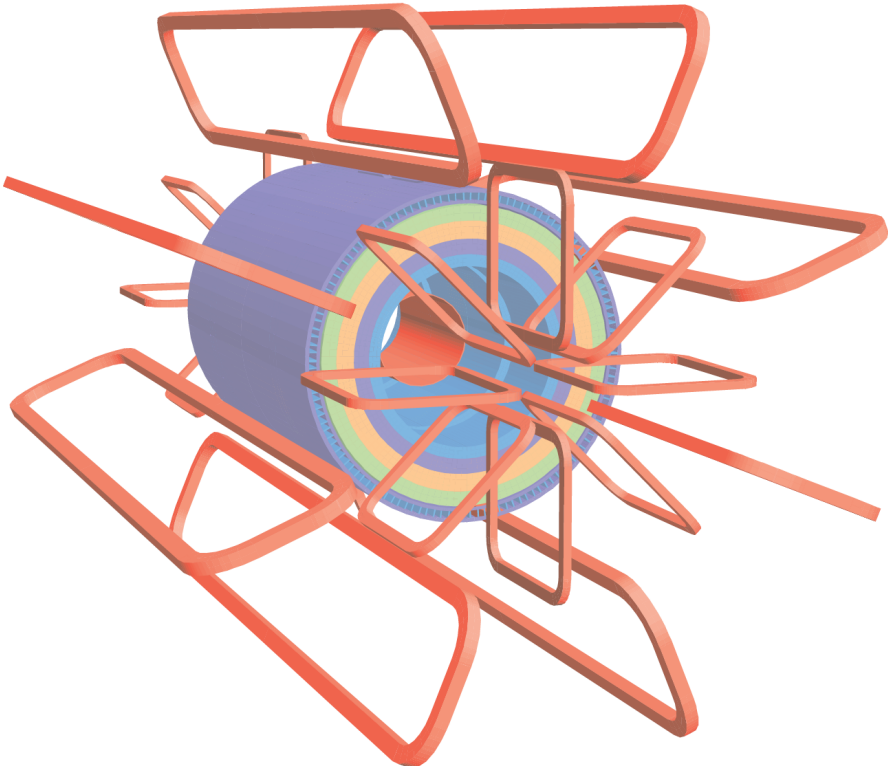


Figure 42: Geometry of ATLAS magnet windings

575 above a designated p_T threshold of 0.5 GeV (in some cases being capable of going as low as 0.1 GeV)
576 within the pseudorapidity range $|\eta| < 2.5$. The inner detector provides reliable electron identification
577 in rapidity range of $|\eta| < 2.0$ for energies from 0.5 GeV to 150 GeV.

578 The ID layout is a result of the technical requirements: it is assembled in a cylindrical envelope of 3512
579 mm in length and 1150 mm in radius. It is surrounded by the magnetic field of 2T imposed by the
580 superconducting solenoid (see section 4.3).

581 Three independent sub-detectors complement each other in the inner detector (see fig. 511a (a)):

582 • Silicon pixel with 3 cylindrical layers for the barrel and 3 discs on each side for the end-cap. It
583 provides the highest granularity around the vertex region. Normally each track hits three pixel
584 layers. The pixel detector has about 80.4 million readout channels. Each of 1744 identical pixel
585 sensors has 47232 pixels and 46080 readout channels. About 90% of the pixels have the size of
586 $50 \times 400 \mu\text{m}^2$, the remaining pixels are a bit longer: $50 \times 600 \mu\text{m}^2$.

587 • Silicon microstrip layers (SCT) with 4 cylindrical layers and 9 discs on each side for the end-cap.
588 A track typically crosses the strip layers in four space points. SCT has approximately 6.3 millions
589 readout channels from its 15912 sensors. There are 768 active strips of 12 cm lenght and $80 \mu\text{m}$
590 width per sensor plus two bias potential strips on the sensor edges.

591 • Transition radiation tracker (TRT) with 73 straw planes in the barrel and 160 straw planes in

592 the end-cap. The TRT has around 351,000 readout channels and detects in average 36 hits per
 593 track. The straw tubes that make up the TRT module are 4 mm thick and 1.44 m long (0.37
 594 m in the endcap) and made out of polyamide films reinforced with carbon fibers. The straws
 595 are filled with gas mixture of 70% Xe, 27% CO₂ and 3%O₂ and supplied with gilded tungsten
 596 anodes which are directly connected to the readout channels. The pixel and SCT sensors are
 597 highly radiation-proof and operate in the temperature range from -5°C to -10°C to minimize the
 598 radiation damage, while the TRT module operates at room temperature.

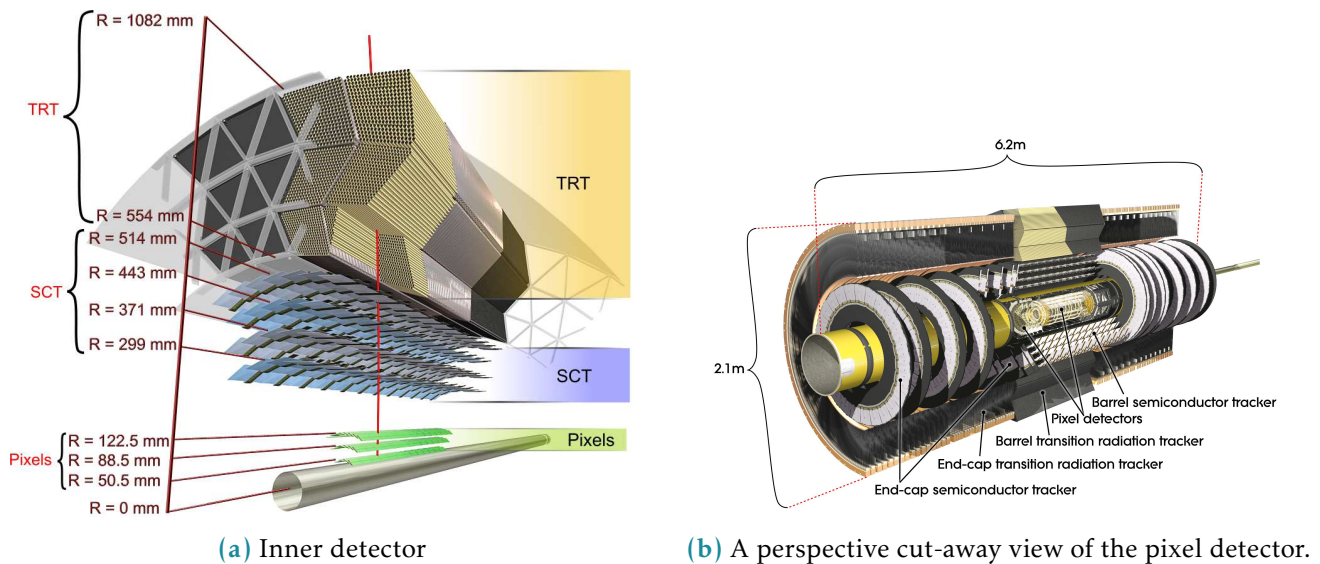


Figure 43: Fichier Gerber des modèles d CFR-34 et CFR-35.

599 4.5 Calorimeter system

600 The ATLAS calorimeter system covers the rapidity range within $|\eta| < 4.9$ and consists of several different
 601 detector systems. A rapidity region matched to the inner detector possesses fine granularity perfectly
 602 suited for high-precision measurements of photons and electrons. The remaining part's granularity is
 603 coarser but enough to perform jet reconstruction and measure E_T^{miss} . The view of ATLAS calorimeter is
 604 presented on fig. 45.

605 Besides measuring the energy of travelling particles calorimeters must also contain electromagnetic and
 606 hadronic showers, limiting their ability to go penetrate the calorimeter completely and get to the muon
 607 chambers. This provides a typical scale for size of the calorimeter modules: the EM calorimeter[6] is
 608 >22 radiation lengths (X_0) in the barrel and $>24X_0$ in the end-caps. The hadronic calorimeter has the
 609 thickness of 9.7 interaction lengths (λ) in the barrel and 10λ in the endcap, which is enough to keep
 610 the leakage level below the typical muon background. This size also provides good resolution for the
 611 E_T^{miss} measuremet. The detailed description of the calorimeter system can be found in the table 41.

- 612 The tile calorimeter[7] uses scintillating tiles as active material alternated with steel absorbers. All the other calorimeter systems use liquid argon as an active medium with lead sampling.

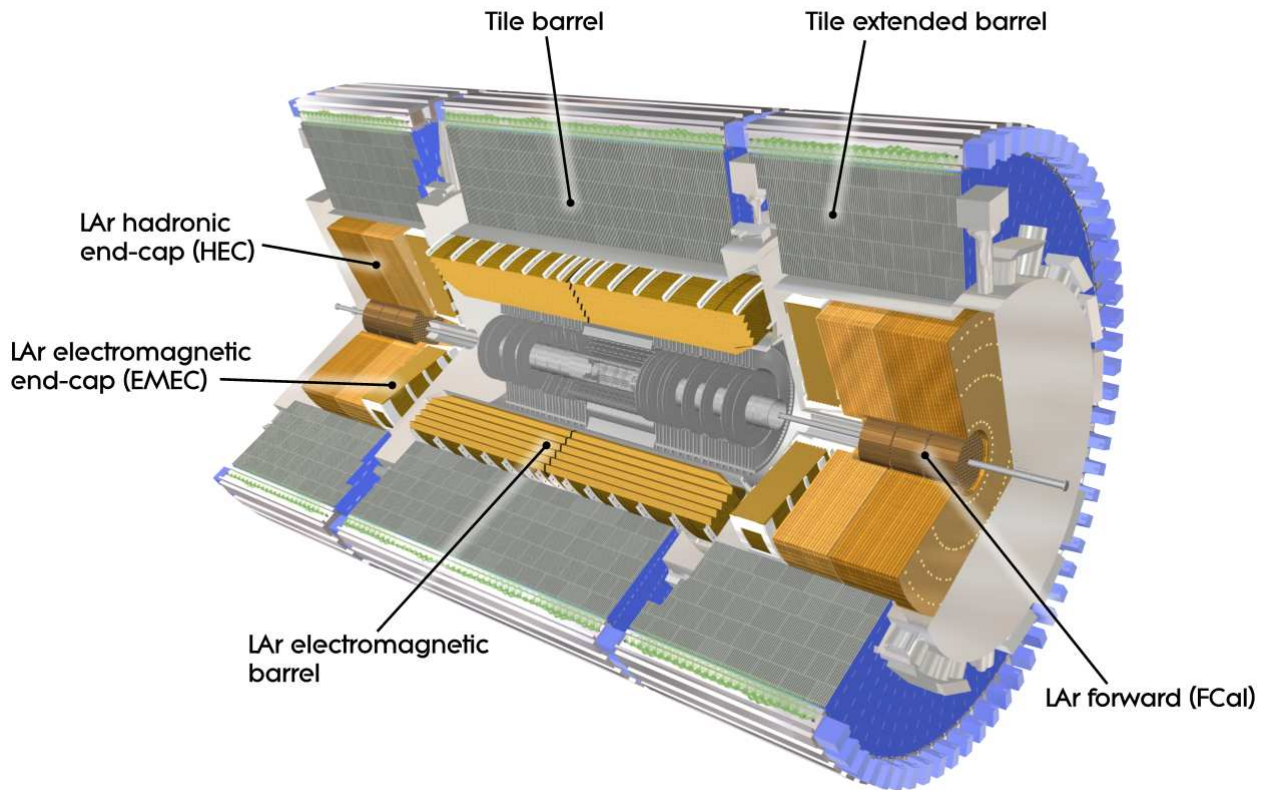


Figure 44: ATLAS calorimeter general layout

613

614 4.5.1 Electromagnetic calorimeter

615 The EMC has two submodules:

- 616 • EMC barrel detector.
617 • Electromagnetic end-cap calorimeter (EMEC) end-cap detector.

618 The EMC barrel module consists of two identical half-barrels 3.2 meters long with inner and outer radii
619 2.8 m and 4 m respectively. There is a 4mm gap at $z = 0$ between the half-barrels. The second crack is
620 situated between the barrel and the end-cap at $1.37 < |\eta| < 1.52$. The EMEC comprises of two pairs of
621 coaxial wheels of 63 cm thick having inner and outer radii of 330 mm and 2098 mm respectively. The
622 crack between the two wheels makes a third crack at $|\eta| = 2.5$. Both barrel and end-cap electromagnetic
623 calorimeters are designed to have an accordion-shaped absorbers made out of lead plates, coated in
624 stainless steel sheets. The readout electrodes are placed in the gaps between the absorbers. This type

	Barrel	End-cap			
EM Calorimeter					
Number of layers and $ \eta $ coverage					
Presampler	1	$ \eta < 1.52$	$1.5 < \eta < 1.8$		
Calorimeter	3	$ \eta < 1.35$	$1.375 < \eta < 1.5$		
Granularity $\Delta\eta \times \Delta\phi$ versus $ \eta $					
Presampler	0.025×0.1	$ \eta < 1.52$	$1.5 < \eta < 1.8$		
Calorimeter 1st layer	$0.025/8 \times 0.1$	$ \eta < 1.40$	$1.375 < \eta < 1.425$		
	0.025×0.025	$1.425 < \eta < 1.5$	$1.425 < \eta < 1.5$		
			$0.025/8 \times 0.1$		
			$1.5 < \eta < 1.8$		
			$0.025/6 \times 0.1$		
			$1.8 < \eta < 2.0$		
			$0.025/4 \times 0.1$		
Calorimeter 2nd layer	0.025×0.025	$ \eta < 1.40$	$1.375 < \eta < 1.425$		
	0.075×0.025	$1.4 < \eta < 1.475$	$1.425 < \eta < 2.5$		
			0.1×0.1		
Calorimeter 3rd layer	0.050×0.025	$ \eta < 1.35$	$1.5 < \eta < 2.5$		
Number of readout channels					
Presampler	7808	1536 (both sides)			
Calorimeter	101760	62208 (both sides)			
LAr hadronic end-cap					
$ \eta $ coverage		$1.5 < \eta < 3.2$			
Number of layers		4			
Granularity $\Delta\eta \times \Delta\phi$		0.1×0.1	$1.5 < \eta < 2.5$		
		0.2×0.2	$2.5 < \eta < 3.2$		
Readout channels		5632 (both sides)			
LAr forward calorimeter					
$ \eta $ coverage		$3.1 < \eta < 4.9$			
Number of layers		3			
Granularity $\Delta x \times \Delta y$		$F\text{Cal } 3.0 \times 2.6$	$3.15 < \eta < 4.30$		
		$F\text{Cal: } \sim\text{four times finer}$	$3.10 < \eta < 3.15$		
			$4.30 < \eta < 4.83$		
		$F\text{Cal2 } 3.3 \times 4.2$	$3.24 < \eta < 4.50$		
		$F\text{Cal2: } \sim\text{four times finer}$	$3.20 < \eta < 3.24$		
			$4.50 < \eta < 4.81$		
		$F\text{Cal3 } 5.4 \times 4.7$	$3.32 < \eta < 4.60$		
		$F\text{Cal3: } \sim\text{four times finer}$	$3.29 < \eta < 3.32$		
Readout channels		$4.60 < \eta < 4.75$			
		3524 (both sides)			
Scintillator tile calorimeter					
	Barrel	Extended barrel			
$ \eta $ coverage	$ \eta < 1.0$	$0.8 < \eta < 1.7$			
Number of layers	3	3			
Granularity $\Delta\eta \times \Delta\phi$		0.1×0.1	0.1×0.1		
		0.2×0.2	0.2×0.1		
Readout channels	5760	4092 (both sides)			

Table 41: ATLAS calorimeter in numbers

625 of geometry allows full coverage in ϕ without cracks together with fast extraction of the signal from
 626 both sides of the electrodes. The orientation of the accordion waves is axial in the barrel and radial in
 627 the end-caps (see fig. 45). These features of the calorimeter lead to virtually uniform performance in ϕ
 628 dimension.

629 Segmentation in η is very different in the layers of the calorimeter, but the second layer always has
 630 the finest granularity because the egamma particles are supposed to leave most of their energy in the
 631 second calorimeter layer. In order to correct for the energy losses upstream the barrel calorimeter is
 632 preceded by a thin LAr active layer of 11mm thick called a presampler. For more details on η coverage
 633 and granularity see table 41.

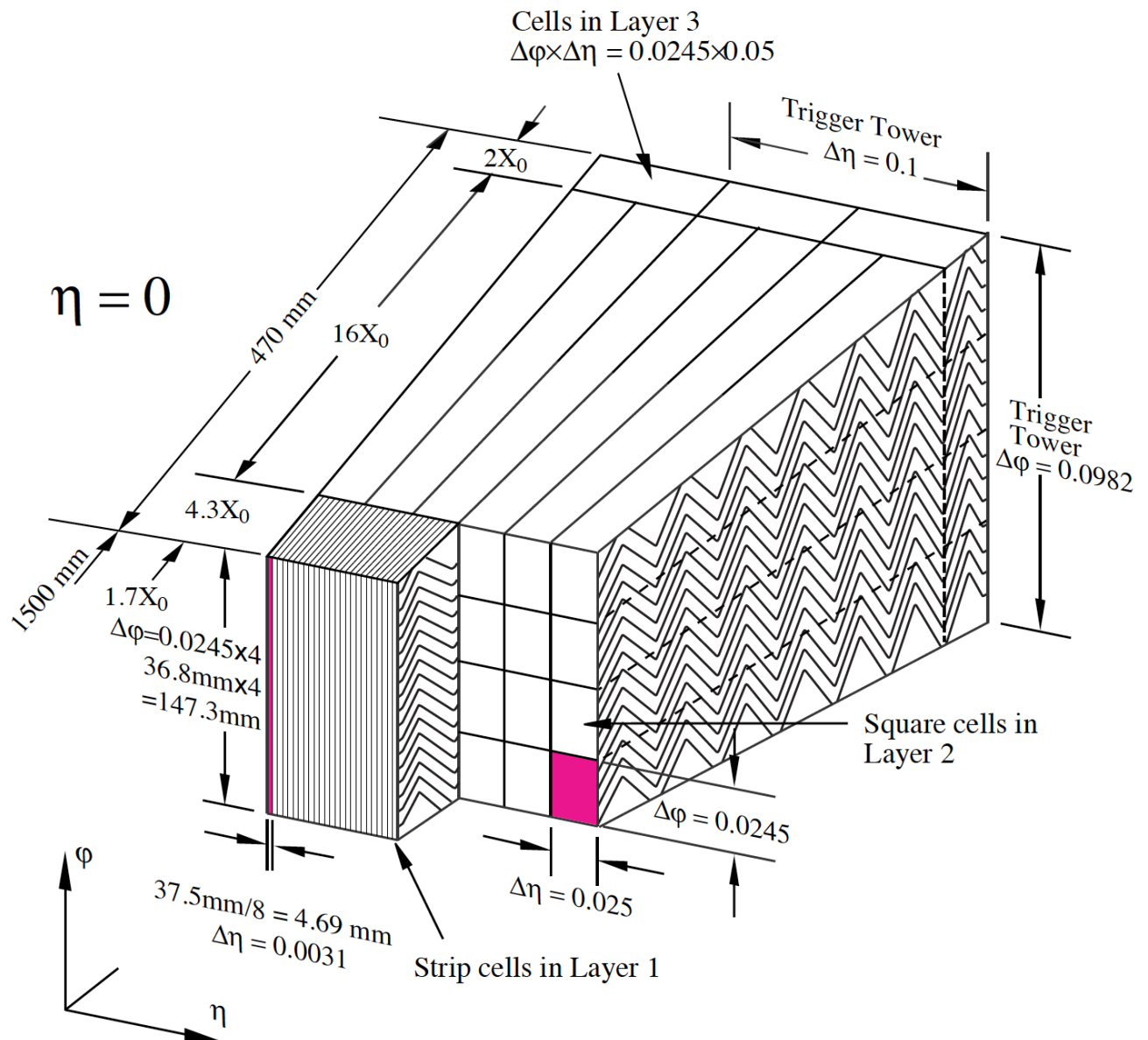
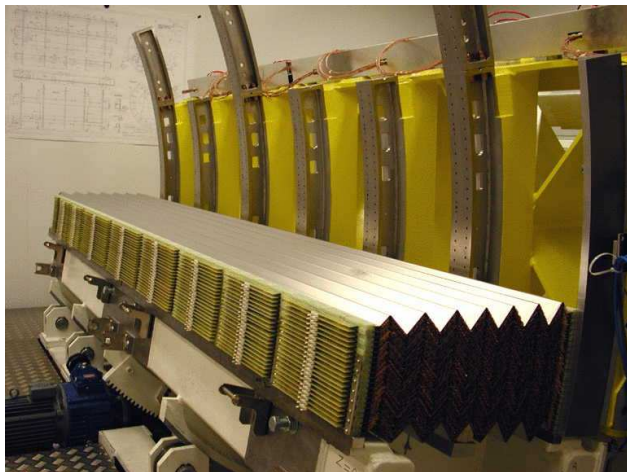


Figure 45: ATLAS EM calorimeter layers



(a) Barrel



(b) End-cap

Figure 46: Accordion absorbers of the EMC

634 4.5.2 Hadronic calorimeter

635 The hadronic calorimeter (HC) is combined of three submodules:

- 636 • HC scintilating tile detector, a steel sampled detector divided in turn into central barrel having
637 5.8 m in length and two extended barrels 2.6 m in length each. The extended barrels have inner
638 radii of 2.28 m and outer radii of 4.25 m. The tile calorimeter consists of three layers having
639 about 1.5, 4.1 and 1.8 interaction lengths λ in the barrel and 1.5, 2.6 and 3.3 λ s in the extended
640 barrel.
- 641 • Hadronic end-cap calorimeter (HEC) detector is a liquid argon calorimeter sampled with copper.
642 It has two pairs of independent wheels symmetrically located behind the EMEC called the frona
643 and the rear wheel. The wheels are cylindrical, their outer radius is 2030mm.
- 644 • Forward calorimeter (FCal) detector modules are located about 4.7 m from the IP and are
645 subjected to very high particle flux and radiation. It consists of three wheels 45 cm deep each.
646 The first one, FCal1 is sampled with copper intended for the measurement of electromagnetic
647 processes. The two other wheels FCal2 and FCal3 are sampled with tungsten and designed for
648 the hadronic showers measurement.

649 The number of the readout channels as well as the η coverage of every module and submodule is
650 described in the Table 41.

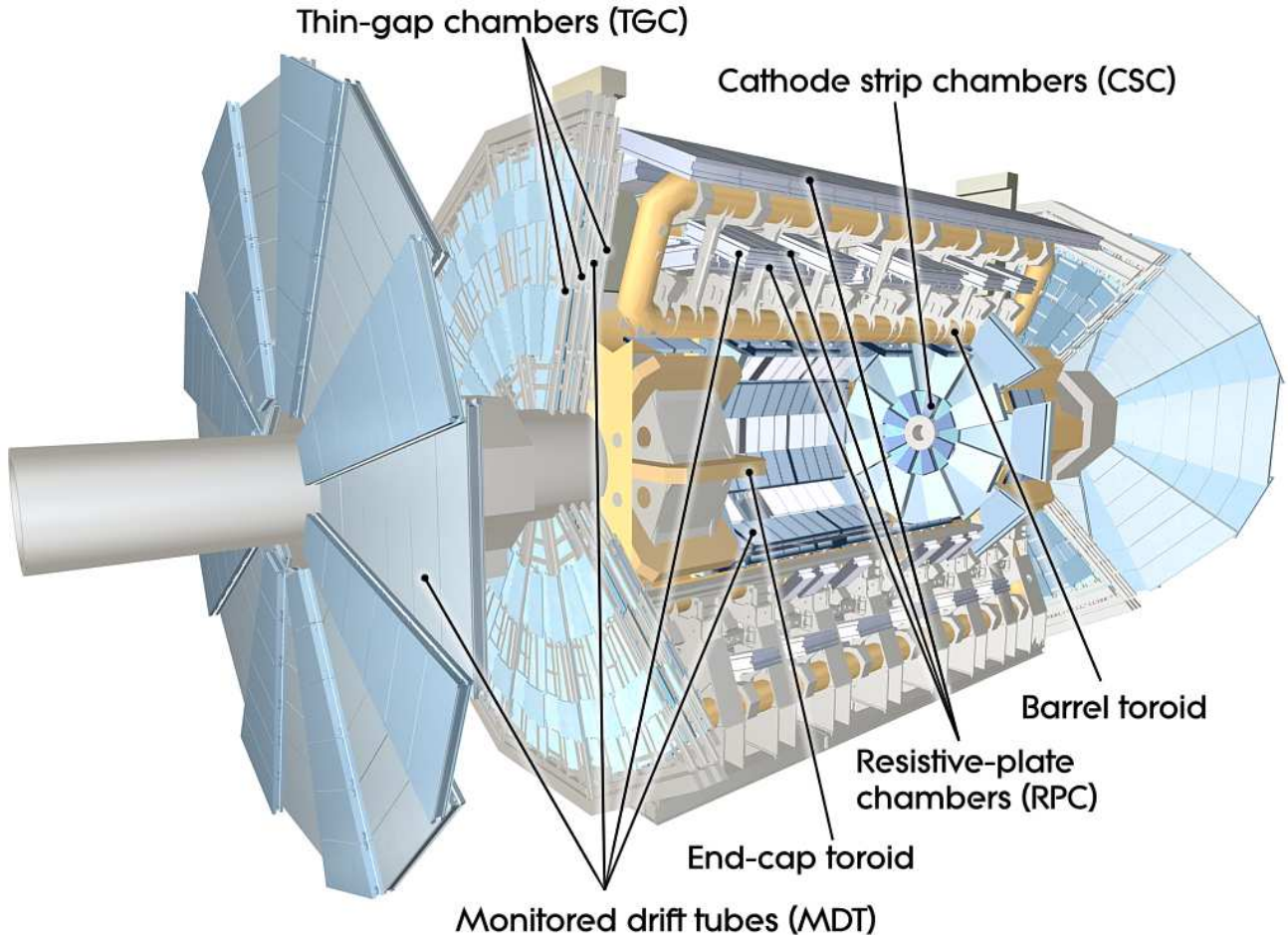


Figure 47: ATLAS muon system

651 4.6 Muon detectors

652 Most of the muons produced as a result of the p-p collisions are able to penetrate through calorimeters
 653 and make it to the muon detectors where their tracks are getting measured. The spectrometer provides
 654 high-precision measurement of the muon momenta in the rapidity range of $|\eta| < 2.7$ and approximate
 655 transverse momentum range of $3 \text{ GeV} < p_T < 3 \text{ TeV}$. The lower bound on the momentum is mainly due
 656 to energy losses in the calorimeter, while the upper bound is caused by the saggita bias coming from
 657 the tracking chambers alignment. The goal p_T resolution is about 10% for a 1 TeV muon track.
 658 The muon tracks[8],[9] are bent by the torroid magnets allowing to determine muon kinematic prop-
 659 erties. The large barrel toroid covers the rapidity range of $|\eta| < 1.4$, while at $1.6 < |\eta| < 2.7$ the tracks
 660 are bent by the smaller end-cap magnets. The deflection in the transition region of $1.4 < |\eta| < 1.6$ is
 661 provided by the barrel and end-cap fields combined.
 662 The general layout of the muon spectrometer is depicted on fig. 47, the parameters of the muon systems
 663 can be found in table ??.

664 the barrel and the end-cap parts.

665 The muon spectrometer possesses a fast triggering system able to trigger for muons in the rapidity
666 range of $|\eta| < 2.4$. It delivers the track information within a few tens of nanoseconds after the particle
667 passage which also allows to use it for the bunch-crossing identification. The trigger chambers measure
668 both η and ϕ coordinates of a track of which the former is in the bending plane and the latter is in the
669 non-bending plane.

670 There are two types of fast triggering detectors used in the muon spectrometer:

- The Resistive Plate Chambers (RPCs) is a gaseous electrode-plate detector filled with a $C_2H_2F_4/Iso-C_4H_{10}/SF_6$ gas mixture (94.7/5/0.3). Two resistive plates of phenolic-melaminic plasctic laminate are separated by insulating spacers of 2 mm thickness. The plates contain an electric field of about 4.9 kV/mm such that the ionizing tracks cause avalanches towards the anode. The signal is read out through the capacitive coupling of metalic strips, mounted to the resistive plates. The RPCs have nominal operating voltage of 9.8 kV and provides an excellent time resolution of a few ns with a supported local rate capability of 1000 Hz/cm^2
- Thin Gap Chambers (TGCs) are multi-wire proportional chambers with the wire-to-cathode ditance of 1.4 mm and wire-to-wire distance of 1.8 mm and wire potential of 2900 V. The 2.8-mm gas gap is filled with highly quenching gas mixture of CO_2 and $n-C_5H_{12}$ (55/45). Small distance between the wires allows a very good time resolution of <25 ns in 99% of cases .

682 The precision-tracking chambers measure the coordinate of a track in the bending plane which is then
683 matched with the second coordinate, measured by the trigger chamber.

684 There are two types of precision tracking systems used:

- The Monitored Drift Tubes (MDTs) are pressurised drift tubes with a diameter of 29.970 mm filled with Ar/CO_2 at 3 bar. Once the muon penetrates the tube it ionises the gas and the ionised electrons are collected at the central tungsten-renium wire of 50 μm in diameter and at a potential of 3080 V. This type of design carries several advantages: mechanical stiffness hence the alignment precision, reliability coming from the fact that a failure of a single tube would not cause malfunction of the others. MDTs counting rate is limited to 150 Hz/cm^2 which is not sufficient for the innermost layer in the forward region of $2.0 < |\eta| < 2.7$.
- Cathode Strip Chambers (CSCs) are gas detectors filled with Ar/CO_2 in 80/20 proportion. The ionised electrons are collected at the wires which are oriented in the radial direction and operate at a potential of 1900 V. They are installed in the so-called Small Wheels and there are 16 CSCs on either side of the ATLAS detector. . The CSCs are able to provide a countng rate of 1000 Hz/cm^2 which makes it a reasonable replacement for the MDTs in the region close to the beam.

697 The precision-tracking chambers in the barrel are positioned between and on the coils of the superconducting
698 barrel thoroid magnet. They form three concentric cylindrical shells around the beam axis

at the approximate radii of 5 m, 7.5 m and 10 m. In the barrel region the RPCs were chosen for the fast triggering whereas the MDTs provide the precision tracking. The end-cap muon spectrometer is assembled in the form of large wheels perpendicular to the beam axis and located at distances about 7.4 m, 10.8 m, 14m and 21.5 m from the interaction point. The triggering in the end-cap is provided by the TGCs. Most of the precision tracking chambers are the MDTs similarly to the barrel, except for the forward region of $2.0 < |\eta| < 2.7$ where the CSCs are installed in the innermost tracking layer. The reason for that is their higher resistance to radiation and increased particle flow which becomes an issue if you get closer to the beam.

Barrel and end-cap alignment is illustrated on fig. 48 which contains the side and transverse views of the muon spectrometer.

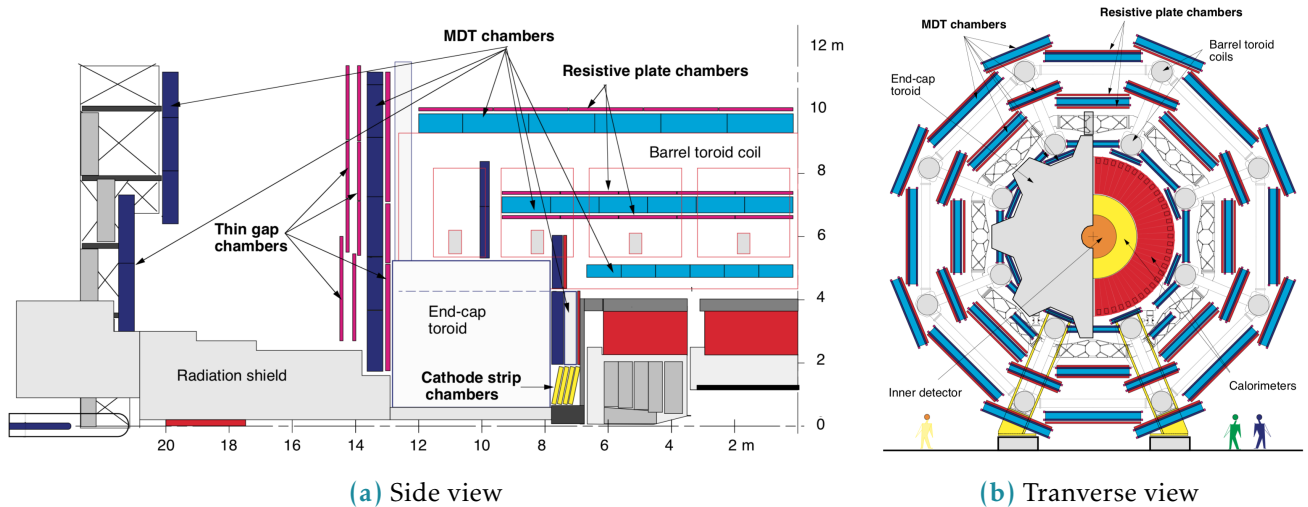


Figure 48: Cut views of the muon systems

708

4.7 Forward detectors

There are three detector systems that cover the ATLAS forward region (see fig. 49): LUminosity measurement using Cherenkov Integrating Detector (LUCID), Zero-Degree Calorimeter (ALFA) and Absolute Luminosity for ATLAS (ZDC). The measurement of luminosity is the main goal of the first two detectors and has fundamental importance: it provides the normalization scale for all the observed processes.

LUCID[10], [11] is the main ATLAS relative luminosity monitor. The main purpose of the LUCID detector is to detect inelastic p-p scattering in the forward region measuring the integrated luminosity and performing online monitoring of the instantaneous luminosity and beam conditions with uncertainty of about few percent. It is symmetrically installed at ± 17 m from the interaction point and at a radial distance of about 10 cm from the beam line (resulting in $|\eta| \approx 5.8$). On each side four bundles of quartz fibers are used as a medium producing Cherenkov radiation directing the Cherenkov light into the 16

Monitored drift tubes	MDT
Coverage	$ \eta < 2.7$ (innermost layer: $ \eta < 2.0$)
Number of chambers	1088 (1050)
Number of channels	339 000 (354 000)
Function	Precision tracking
Cathode strip chambers	CSC
Coverage	$2.0 < \eta < 2.7$
Number of chambers	32
Number of channels	31 000
Function	Precision tracking
Resistive plate chambers	RPC
Coverage	$ \eta < 1.05$
Number of chambers	544 (606)
Number of channels	359 000 (373 000)
Function	Triggering, second coordinate
Thin gap chambers	TGC
Coverage	$1.05 < \eta < 2.7$
Number of chambers	3588
Number of channels	318 000
Function	Triggering, second coordinate

Table 42: ATLAS muon spectrometer subsystems coverage and parameters

- 721 Photomultipliator Tubes (PMTs) placed outside the radiation shielding.
- 722 The ALFA[12] detector is used to measure the absolute luminosity through elastic scattering at small
723 angles. In order to perform such measurement we need to meet the following conditions:
724
- 725 • The beam has to be more parallel than normally. Special collider beam optics allowing high values
726 of the amplitude function at the interaction point β^* together with reduced beam emittance.
- 727 • To be sensitive to small angles the detectors have to be placed as far as possible from the
728 interaction point and close to the beam. This is why the detectors are located inside the Roman
729 pots at ± 240 from the interaction point. On each side there are two Roman pots separated by
730 four meters.
- 731 The Roman pot windows allow the elastically scattered protons reach the square scintillating fibres of
732 0.5 mm width which are in turn connected to multi-anode PMTs through the light-guides. The detector
733 provides a spacial resolution of $30 \mu\text{m}$ and allows to measure absolute luminosity with uncertainty of
734 1.7% for the Run 2[13].
- 735 ZDC are used to detect forward neutrons at $|\eta| > 8.3$ in heavy-ion collisions, which in turn allows to
736 determine the centrality of such collisions. The detector is installed at ± 140 m from the interaction

737 point. Every ZDC arm consists of 4 modules: one electromagnetic and three hadronic. These modules
 738 are quartz rods shielded by the tungsten plates and connected to the PMTs via the light-guides allowing
 739 to measure incending particle energy and position. The EM module has a better position resolution
 740 mapping each of 96 quartz rods into a single pixel, while the hadronic modules map a bundle of four
 741 rods into a pixel. Only one of the three hadronic modules per arm provide position-sensing rods and
 only the arm at -140 m has the position-sensing EM module.

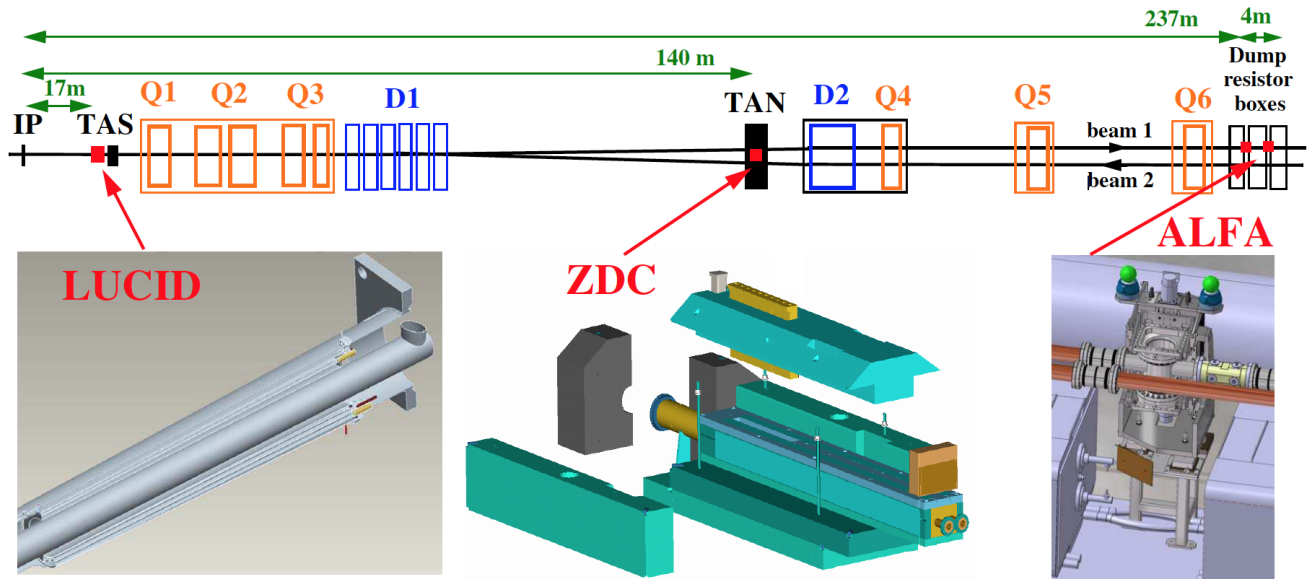


Figure 49: ATLAS forward detectors

742

743 4.8 Trigger system

744 Considering that the bunch crossing rate at LHC is about 40 MHz and that ATLAS detector has over
 745 one million read-out channels it would never be possible to store all the raw data without significant
 746 preselection that would decrease the data rate. The selection criteria are picked to retain and store only
 747 the events which might be interesting for the LHC physics. The preselection and storage is conducted
 748 with the help of TDAQ systems.

749 The trigger system has three distinct levels: L1, L2 and the event filter, the two latter levels are also
 750 called High-level Trigger (HLT). Each next level refines the decisions made before and, if necessary,
 751 applies additional selection, further lowering the event rate. The data acquisition system receives and
 752 buffers the event data from the readout electronics at the L1 trigger accept rate which for Run 2 is
 753 about 100 kHz [14]. The HLT then lowers the rate down to 1.5 kHz which is then stored for the offline
 754 analysis.

755 The L1 trigger looks for muons, electrons, photons, jets at hadrons from τ -lepton decays with high
 756 transverse momentum, large missing and total transverse energy. The muons of interest are identified

757 using the muon spectrometer trigger system described in section 4.6. The rest of the particles are
 758 selected using the information from all the calorimeters with reduced granularity. During the Run 2 an
 759 intermediate L1Topo trigger was also added allowing to combine the information from the spectrometer
 760 and calorimeter and extend possible trigger selections. Results from these triggers gets processed by
 761 the central trigger processor which implements the trigger menu made up of different combinations of
 762 trigger selections. The decision latency for the L1 trigger must not exceed $2.5 \mu\text{s}$ after the corresponding
 763 bunch crossing.

764 For every selected event the L1 defines one or more regions called Region of Interest (RoI) which
 765 include the η and ϕ coordinates of these regions for their subsequent use by the HLT. The L2 selection
 766 is seeded RoI and uses full granularity and precision along with other detector data available. The
 trigger block diagram is presented in fig. 410.

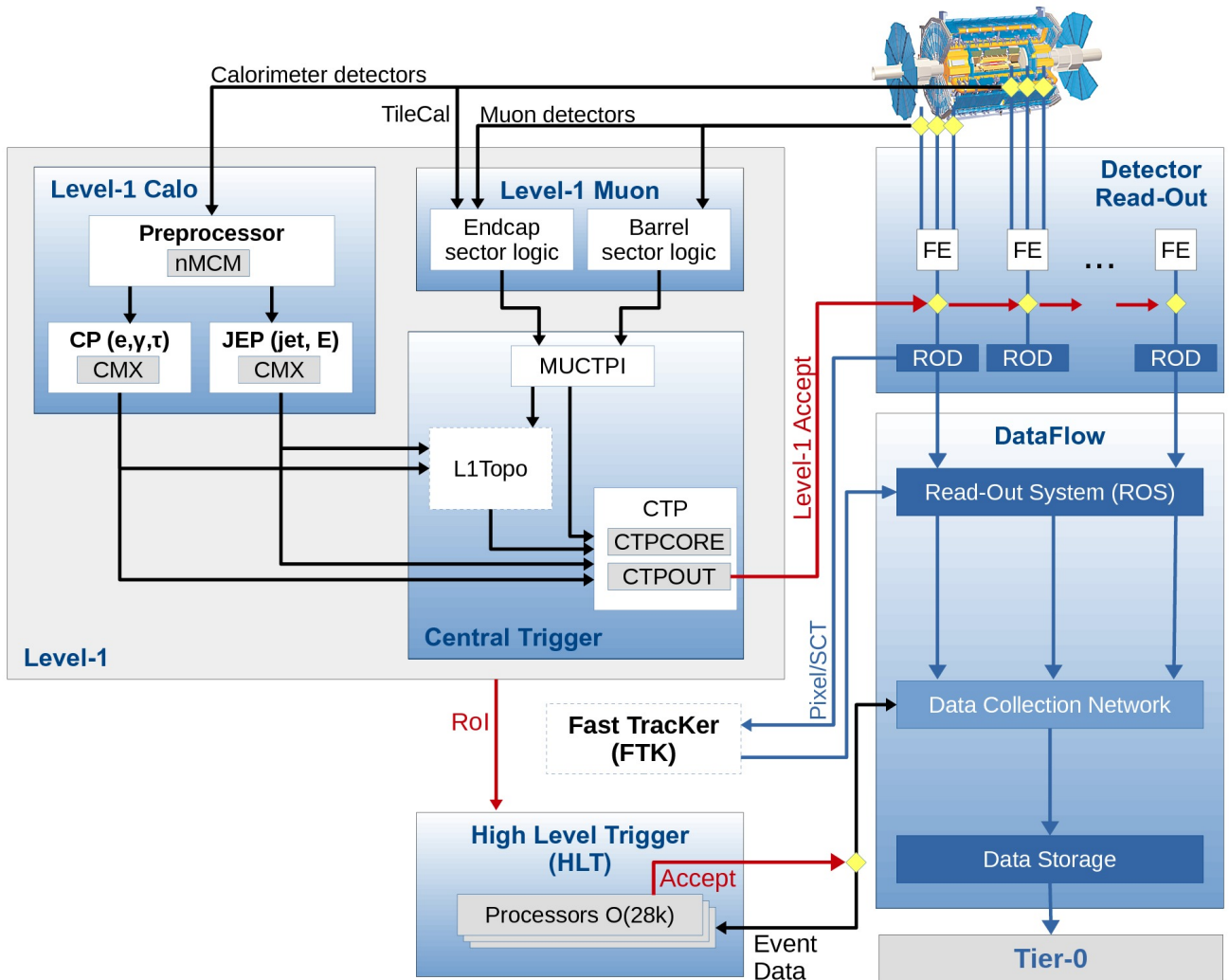


Figure 410: The scheme of ATLAS trigger systems

768

769

Electromagnetic shower shapes correction in the electromagnetic calorimeter

770 “Potentielle citation sans aucun rapport avec le sujet”

⁷⁷¹ — Personne inconnue, contexte à déterminer

772 5.1 Introduction

773 The design and functionality of the ATLAS electromagnetic calorimeter was described in 4.5.1. Let's
774 consider a bit more in detail the physical processes happening in the EMC.

775 It order to measure particle's energy within the calorimeter we must make the particle to loose its entire
776 energy within the calorimeter. For the electrons and photons with energies over few MeV (which is the
777 case for the ATLAS experiment) the primary energy loss mechanism lies in bremsstrahlung radiation
778 and pair creation). The two processes complete each other, so when a high-energy electron or photon
779 gets into the calorimeter, it creates an avalanche-like processus called the electromagnetic shower when
780 a bremsstrahlung-radiated photons create more electron-positron pairs which in turn radiate more
781 bremsstrahlung photons and so on and so forth (see fig. 51.)

The longitudinal and transverse development of the shower depends on the type of the initial particle

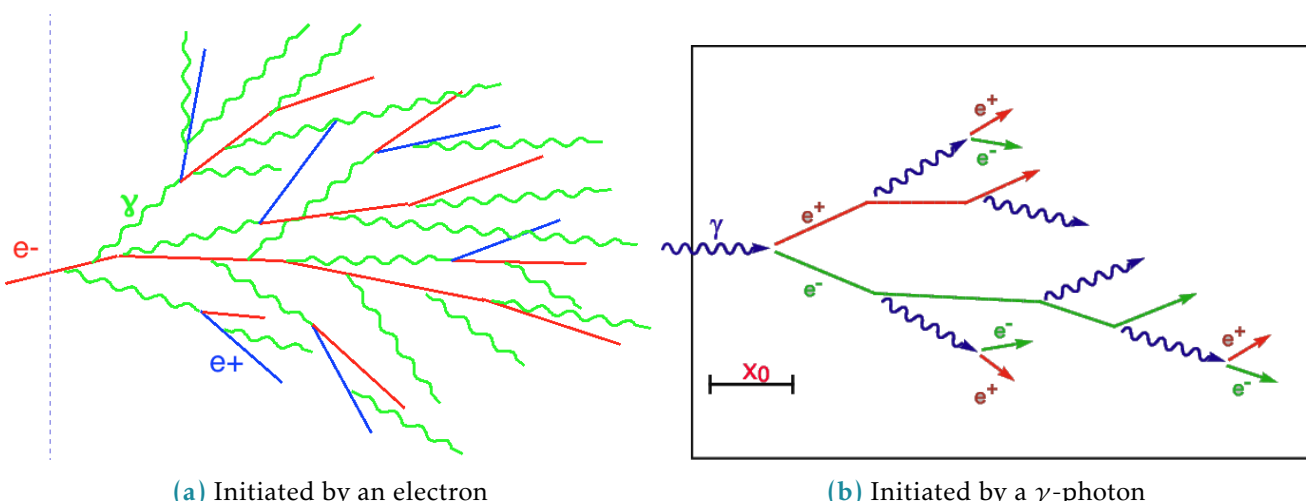
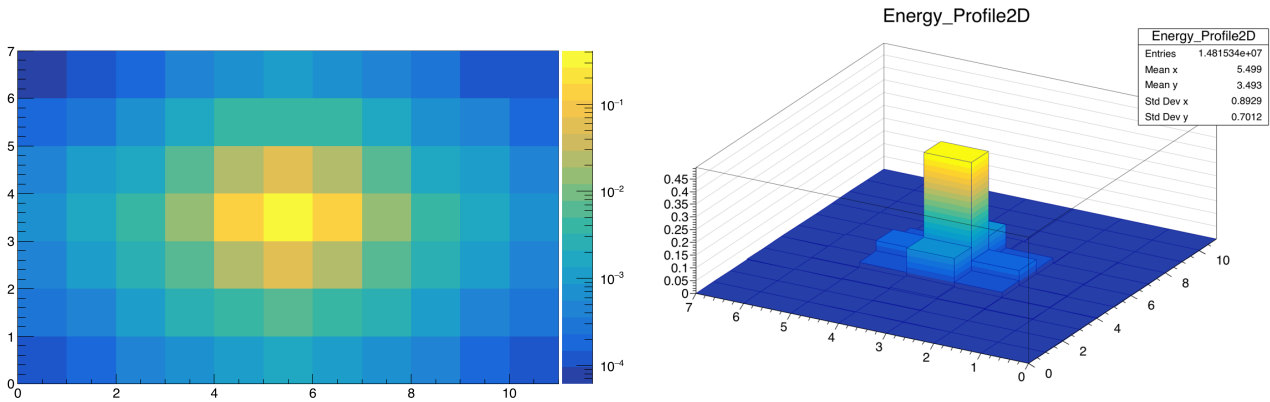


Figure 51: The schematic portrayal of EM shower development

782

and on its energy. The energy is well measured by the calorimeter, but identifying the particle still remains a challenging task. The transverse granularity of the ATLAS calorimeter allows to resolve the

785 energy distribution within the electromagnetic shower in the transverse plane. This information can
 786 later be used for particle identification.
 787 When an e/ γ particle hits the calorimeter its footprint in the second layer of the calorimeter is visible as
 788 a cluster of calorimeter cells centered at the central cell having the most energy deposited (sometimes
 789 referred to as "the hottest cell"). Roughly 90% of shower energy is contained in the core 3x3 cells. We
 790 have considered a cluster of 7x11 ($\eta \times \phi$) cells, which is schematically depicted on fig. 52a.

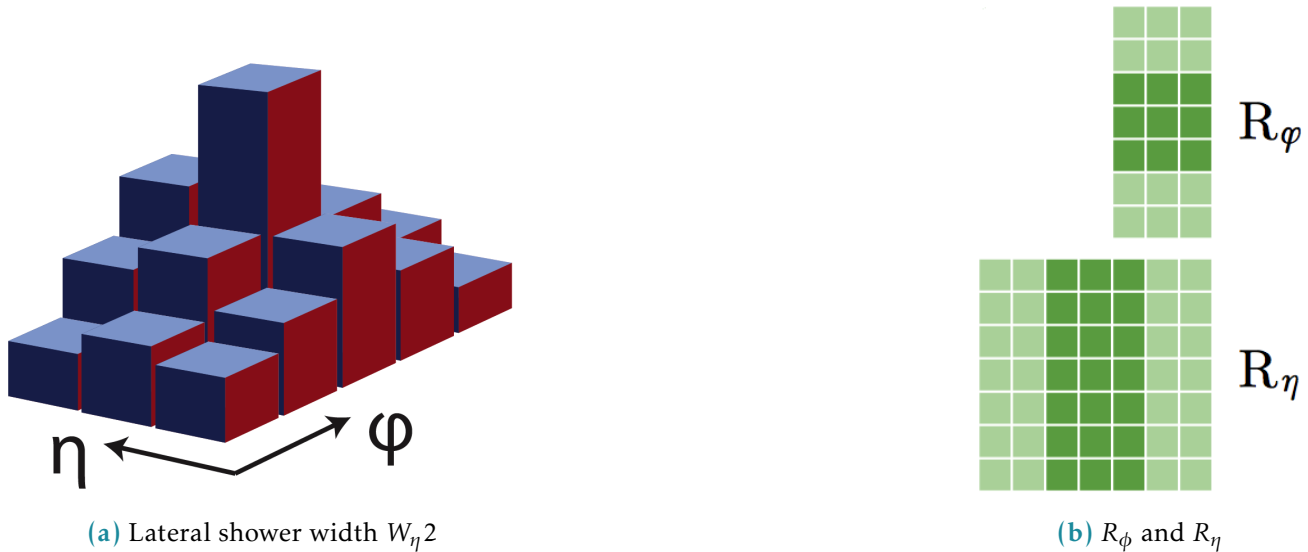


(a) Energy profile of a window of 7x11 cells in the 2nd calorimeter layer (logarithmic scale)

(b) 2D profile of the cluster

Figure 52: Visualisations of the 7x11 calorimeter cluster

791 In order to characterise the energy distribution within the shower profile a number of observables
 792 called shower shapes are used. They are then used as an input for particle identification MVA algorithm.
 793 Current study focuses on the second layer of the calorimeter for which there are three shower shape
 794 observables described below [1]:



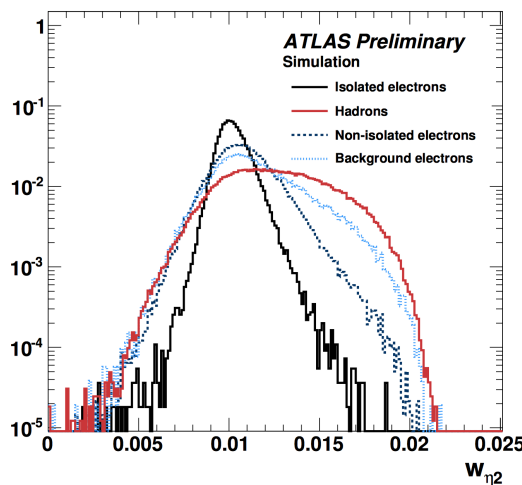
(a) Lateral shower width $W_\eta/2$

(b) R_ϕ and R_η

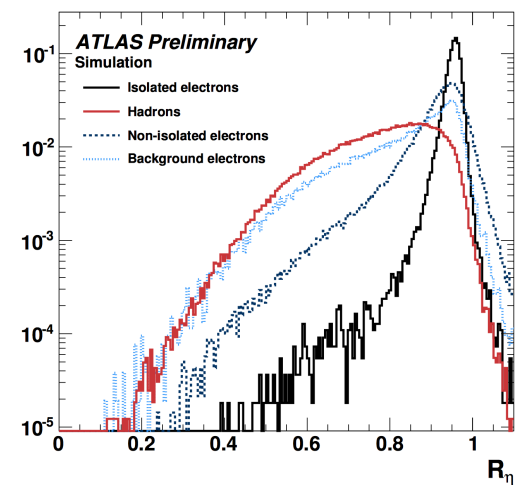
Figure 53: Shower shapes in the second layer of the electromagnetic calorimeter

- 795 • Lateral shower width $W_{\eta 2} = \sqrt{\sum(E_i \eta_i^2) - (\sum(E_i \eta_i)/\sum(E_i))^2}$ calculated within a window of 3x5
796 cells.
- 797 • R_ϕ - ratio of the energy in 3x3 cells over the energy in 3x7 cells centered around the hottest cell.
- 798 • R_η - ratio of the energy in 3x7 cells over the energy in 7x7 cells centered around the hottest cell.

799 The shower shapes distributions for different types of particles is shown in fig. ?? - although the
800 distributions overlap, combining the shower shapes information with the inputs from other detectors
allow to identify the particle.



(a) $W_{\eta 2}$ distribution simulation



(b) R_η distribution simulation

Figure 54: Distribution of R_η in simulation (GEANT4) for electrons and jets [2].

801
802 Figure ?? shows how R_η distribution is different in jets, signal electrons and background electrons.
803 Background electrons denote non-prompt electrons which are not originated from primary vertex.
804

805 The shower shapes appear to be extremely sensitive to the detector material modelling. A sim-
806 plification in the geometry of the EMCAL absorber geometry in GEANT4 9.2 (a layered structure of
807 the accordion was represented as a homogenous material) has lead to visible discrepancies in the
808 shower shapes between the data and MC. This was corrected in GEANT4 9.4 significantly improving
809 the agreement, although not eliminating it completely (see fig. 55). The origin for the remaining
810 discrepancy is not clear.

811
812 Disagreement in shower shapes between the data and MC leads to discrepancies in particle ID which
813 are later fixed using η - and p_T -dependent scale factors. Correction of the shower shapes aims to get
814 the scale factors closer to unity, reducing the corresponding systematic uncertainties and improving
815 the precision of the measurements with electrons in the final states.

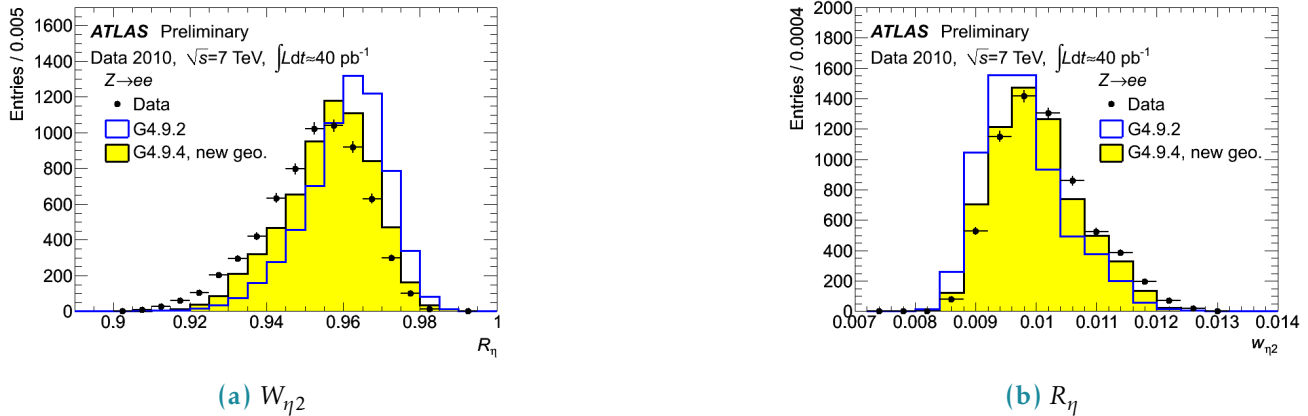


Figure 55: Data/MC Comparison for Calorimeter Shower Shapes of High Et Electrons [3].

816 5.2 Shower shapes measurement and correction

817 5.2.1 Event selection

818 For this study we have considered electrons from the $Z \rightarrow ee$ decay. A set of recommended single
 819 electron triggers was used (HLT_e26_lhtight_nod0_ivarloose, HLT_e60_lhmedium_nod0,
 820 HLT_e140_lhloose_nod0, HLT_e300_etcut). Each event was required to have 2 electrons at least one
 821 of which has $p_T > 25$ GeV. In order to suppress the background both electrons had to pass gradient
 822 isolation. Z invariant mass cut was applied with a window of 80 – 120GeV. To avoid identification bias
 823 from triggering the tag and probe approach was used with only probe electrons taken into consideration
 824 [4]. The electron cluster in the second calorimeter layer was required to contain information from 77
 825 calorimeter cells. No pile-up reweighting has been applied. Datasets of 264786295 events in data (2017
 826 proton-proton collisions) and 79340000 events in MC (Powheg+Pythia8) were used.

827 5.2.2 Data/MC discrepancies

828 Our consideration begins with the energy deposit of an electron in the second layer of the calorimeter.
 829 A window of 7 cells in η and 11 cells in ϕ is centered around the cell with the highest energy.

830 Shower shapes were considered in 14 η bins in the range between $|\eta| = (0, 2.4)$ in order to investigate
 831 how the discrepancy depends on η .

832 The η -dependent shower shapes in data are wider than the MC and show a larger discrepancy in the
 833 endcap ($|\eta| = (1.52, 2.4)$). For ϕ dimension the situation is the opposite: MC is wider than the data and
 834 the barrel ($|\eta| = (0, 1.52)$) shows larger discrepancy. Figures ??, ??, ?? contain examples of shower shapes
 835 in different eta bins.

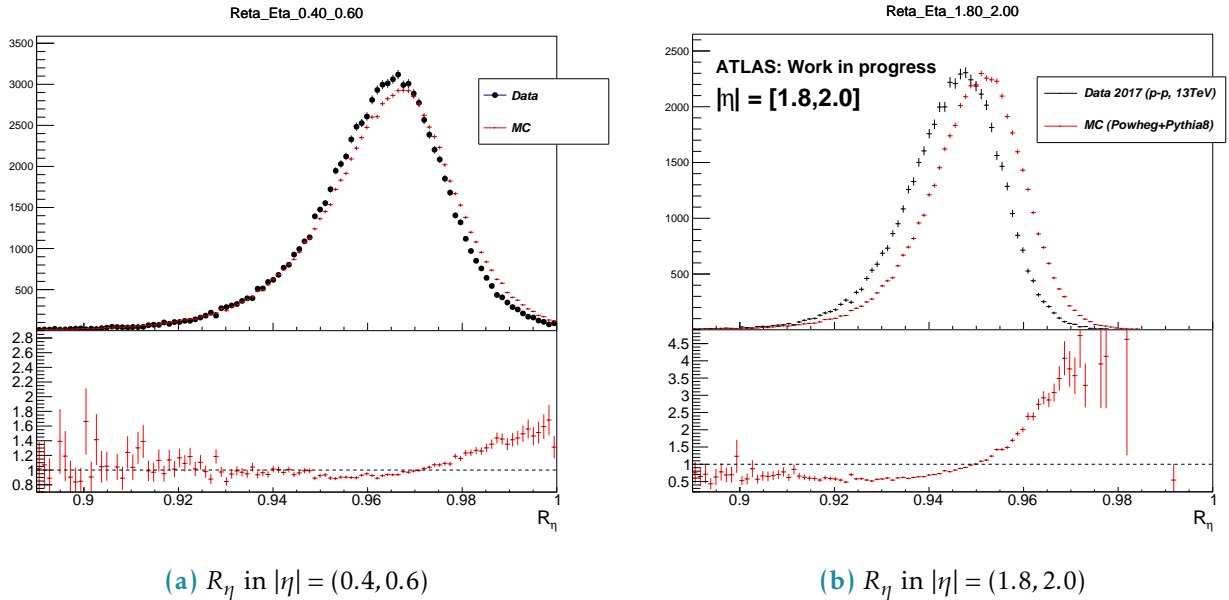


Figure 56: R_η in the barrel and in the end-cap, Data vs MC

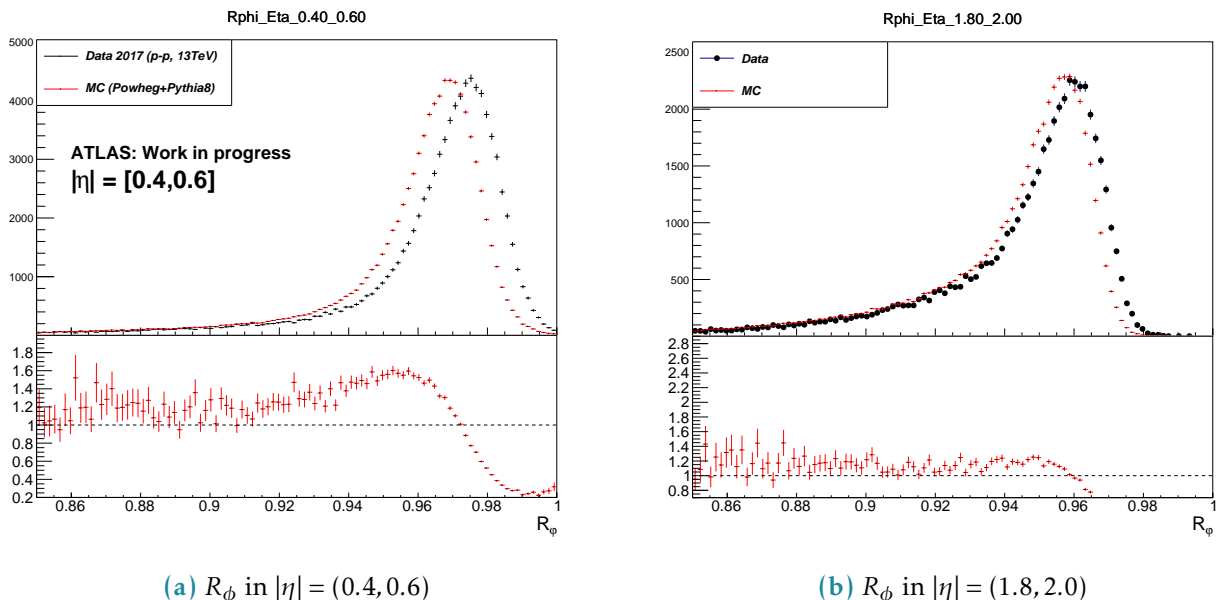


Figure 57: R_ϕ in the barrel and in the end-cap, Data vs MC

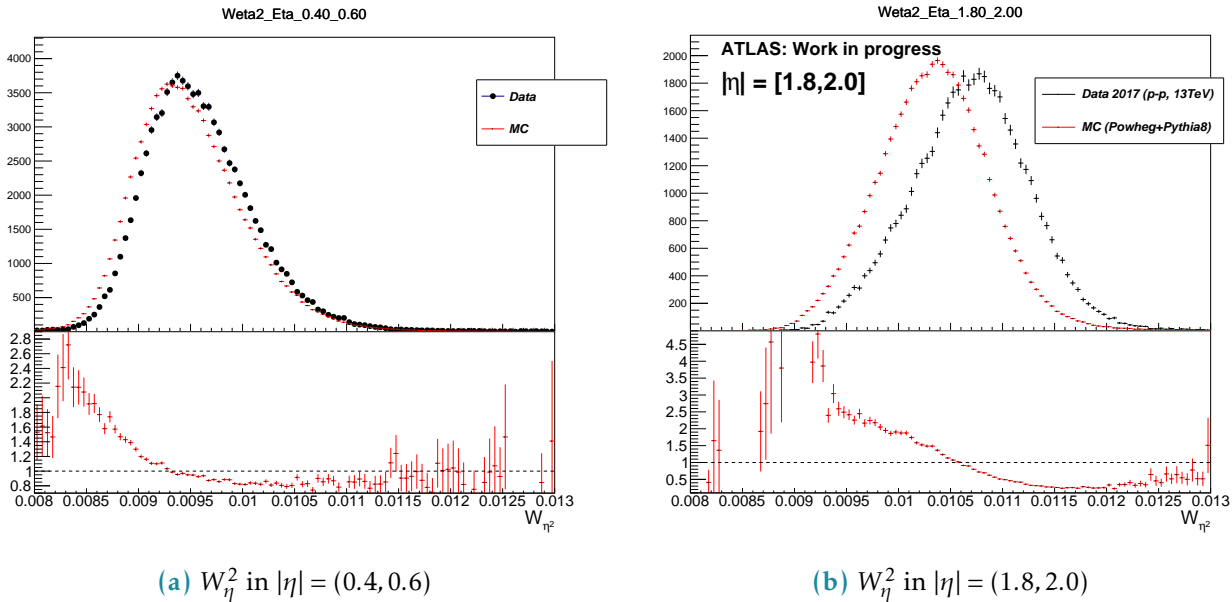


Figure 58: W_η^2 in the barrel and in the end-cap, Data vs MC

836 5.2.3 The correction procedure

837 The correction matrix

838 The correction procedure is based on the redistribution of energy between the cluster cells in MC so
 839 that the distribution becomes consistent with the data. For every η bin a correction matrix is derived in
 840 the following way:

$$M_i^{Correction} = \frac{E_i^{Data}}{\sum E^{Data}} - \frac{E_i^{MC}}{\sum E^{MC}}$$

841 $\sum_i M_i^{Correction} = 0, i = 1..77.$

842 E_i^{Data}, E_i^{MC} - matrix elements of the averaged energy profiles. The correction is then applied to the
 843 electron cluster cells on event-by-event basis:

$$E_i^{Reweighted} = E_i^{Non-reweighted} (1 + M_i^{Correction}).$$

844 This redistributes the energy among the cells keeping the total energy exactly the same.

845 Bremsstrahlung tails

846 The magnetic field directed along the ϕ dimension leads to a significant asymmetry in energy deposits
 847 for electrons and positrons (figure ??).

848 Considering the fact that the reweighting is intended to correct for the data/MC discrepancies
 849 themselves and not for the bremsstrahlung effect it makes sense to develop the bremsstrahlung-free
 850 correction function based on e^+ and e^- correction matrices. The principle is schematically explained on

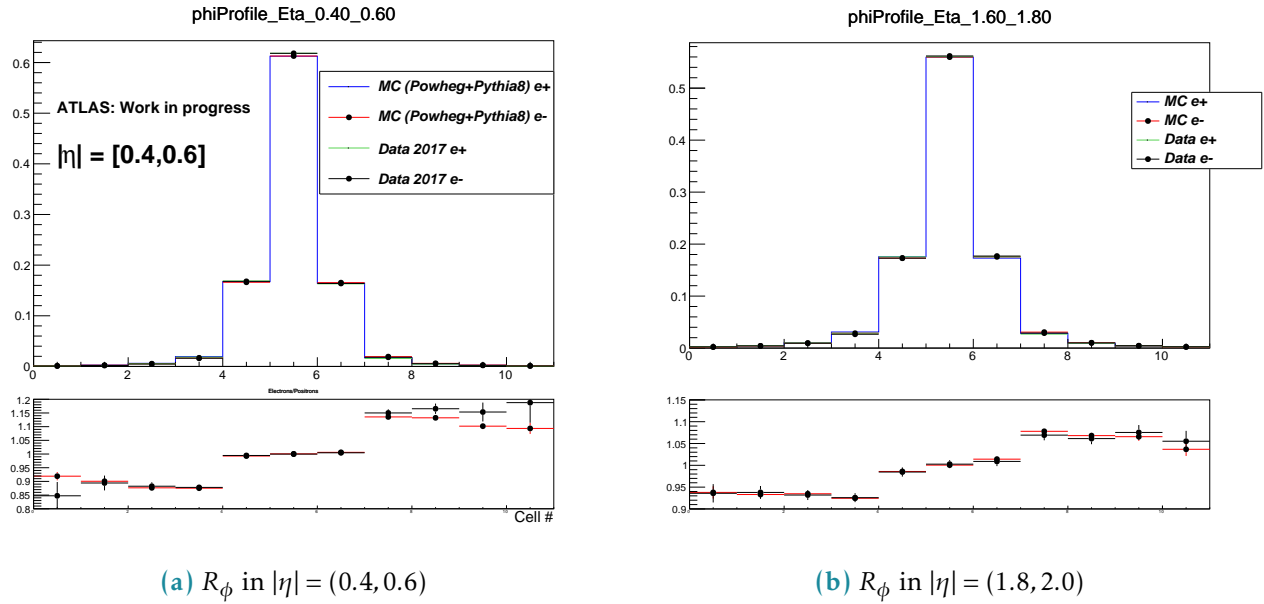


Figure 59: R_ϕ in the barrel and in the end-cap, Data vs MC

851 figure 510.

Good agreement of data and MC description of e^+ and e^- asymmetry gives a hint that the material

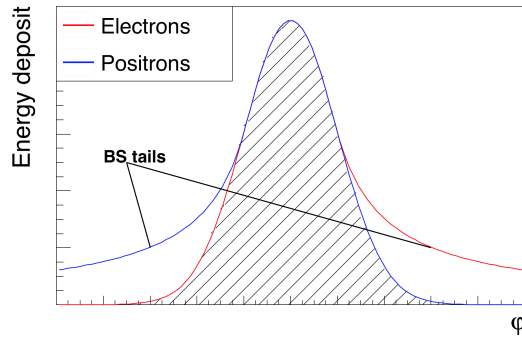


Figure 510: Schematic energy profile in ϕ dimension. Bremsstrahlung tails subtraction based on e^+ and e^- energy profiles.

852

853 mismodelling cannot be the main source of the data/MC disagreement.

854

855 5.3 Results

856 Figures 511, 512, 513 show the effect of the correction. The shower shapes in MC become very close to
857 the data, correcting a significant discrepancy.

858 Figures 514 contain shower shapes vs p_T integrated over η . They demonstrate that the correction does

not depend on the p_T which allows to expect the decreased systematic uncertainties for p_T regions distant from 40 – 50 GeV.

Finally, figure 515 shows the effect of the correction on electron ID efficiency. We can see a visible improvement, notably in the endcap region. Nevertheless the barrel region shows little improvement. It can be explained by the fact that electron ID MVA relies on many variables while only a number of them were corrected during current study.

The proposed method is getting integrated into ATLAS Athena framework as an option and is planned to be used as a baseline for Run 3.

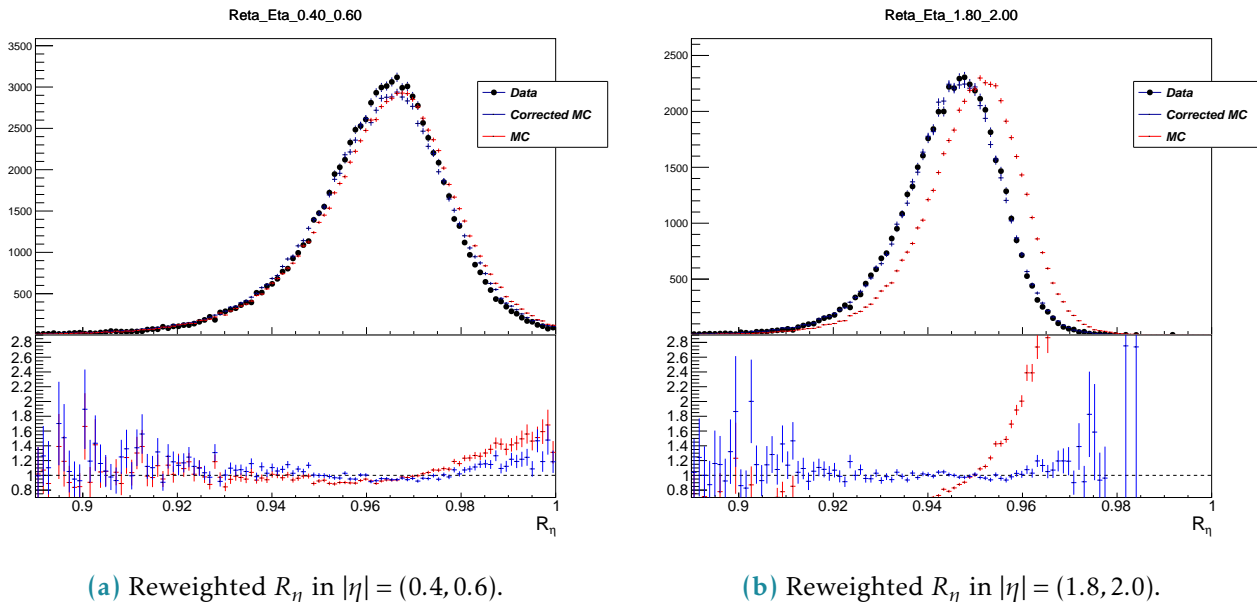


Figure 511: R_η in the barrel and in the end-cap

5.4 Appendix: control plots

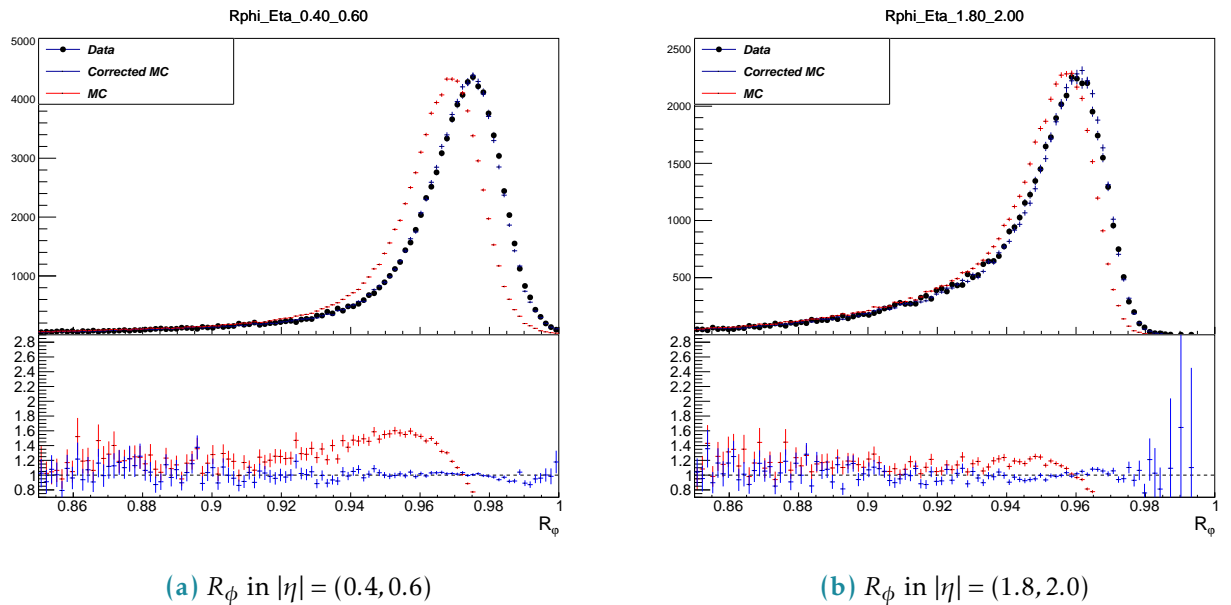


Figure 512: R_ϕ in the barrel and in the end-cap, Data, MC, reweighted MC

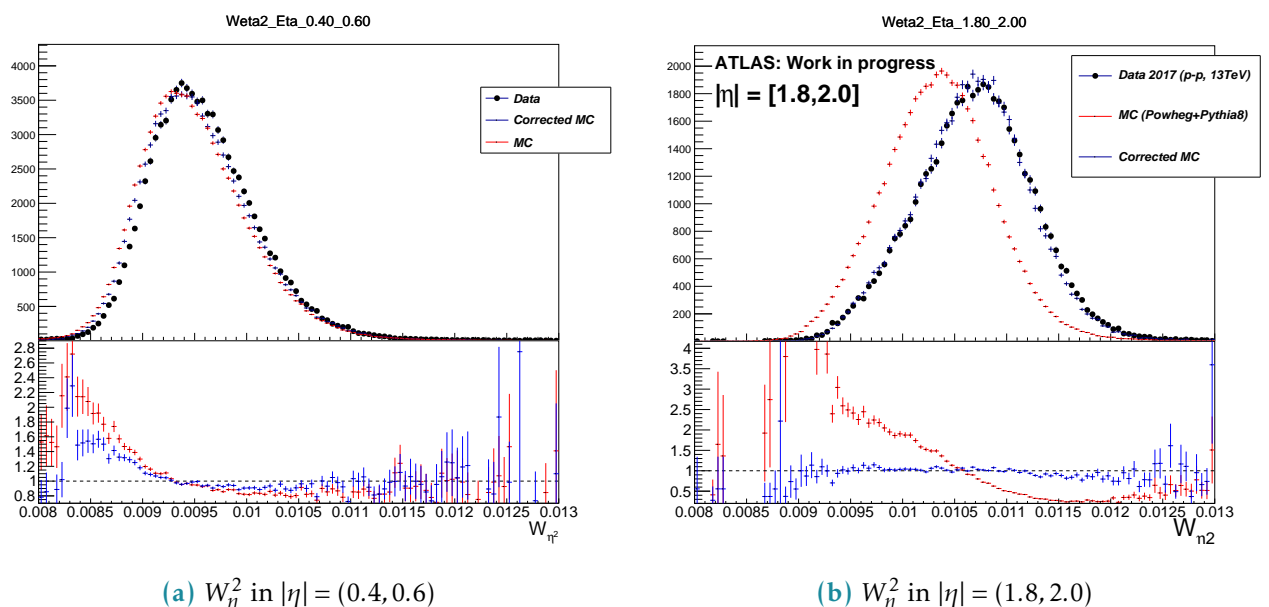


Figure 513: W_η^2 in the barrel and in the end-cap, Data, MC, reweighted MC

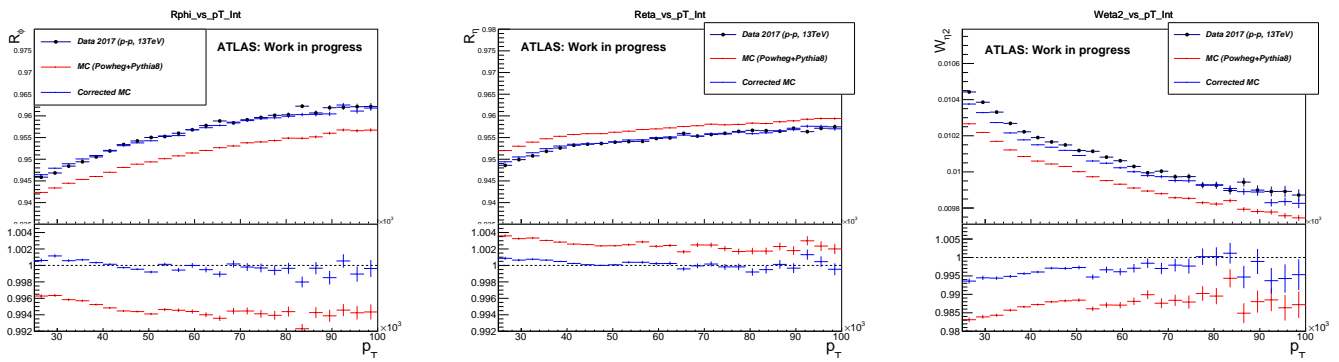


Figure 514: Distributions integrated over p_T (a) R_{ϕ} ; (b) R_{η} ; (c) $W_{\eta 2}$.

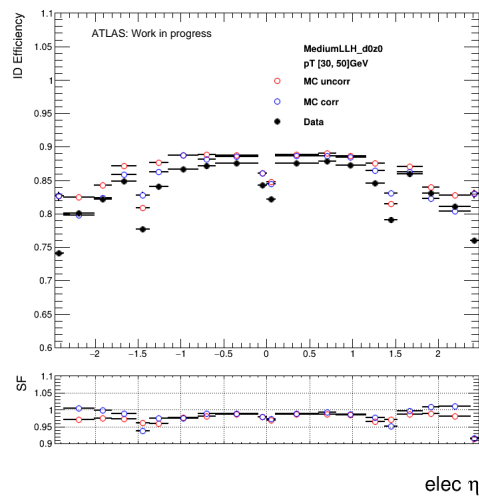


Figure 515: Electron identification efficiency as a function of the electron pseudo-rapidity

868 Bibliography

- 869 [1] “Electron and photon performance measurements with the ATLAS detector using the 2015-2017
870 LHC proton-proton collision data”. In: *JINST* 14.arXiv:1908.00005. 12 (Aug. 2019). 31 figures,
871 3 tables. All figures including auxiliary figures are available at <https://atlas.web.cern.ch/Atlas/GROUPS/PHYSICS/PAPERS/EGAM-2018-01>, P12006. 70 p. doi: 10.1088/1748-0221/14/12/P12006. URL: <https://cds.cern.ch/record/2684552>.
- 874 [2] *Expected electron performance in the ATLAS experiment*. Tech. rep. ATL-PHYS-PUB-2011-006.
875 Geneva: CERN, Apr. 2011. URL: <http://cds.cern.ch/record/1345327>.
- 876 [3] *Data/MC Comparison for Calorimeter Shower Shapes of High Et Electrons*. Tech. rep. ATL-COM-
877 PHYS-2011-1299. Geneva: CERN. URL: <https://atlas.web.cern.ch/Atlas/GROUPS/PHYSICS/EGAMMA/PublicPlots/2011005/ATL-COM-PHYS-2011-1299/index.html>.

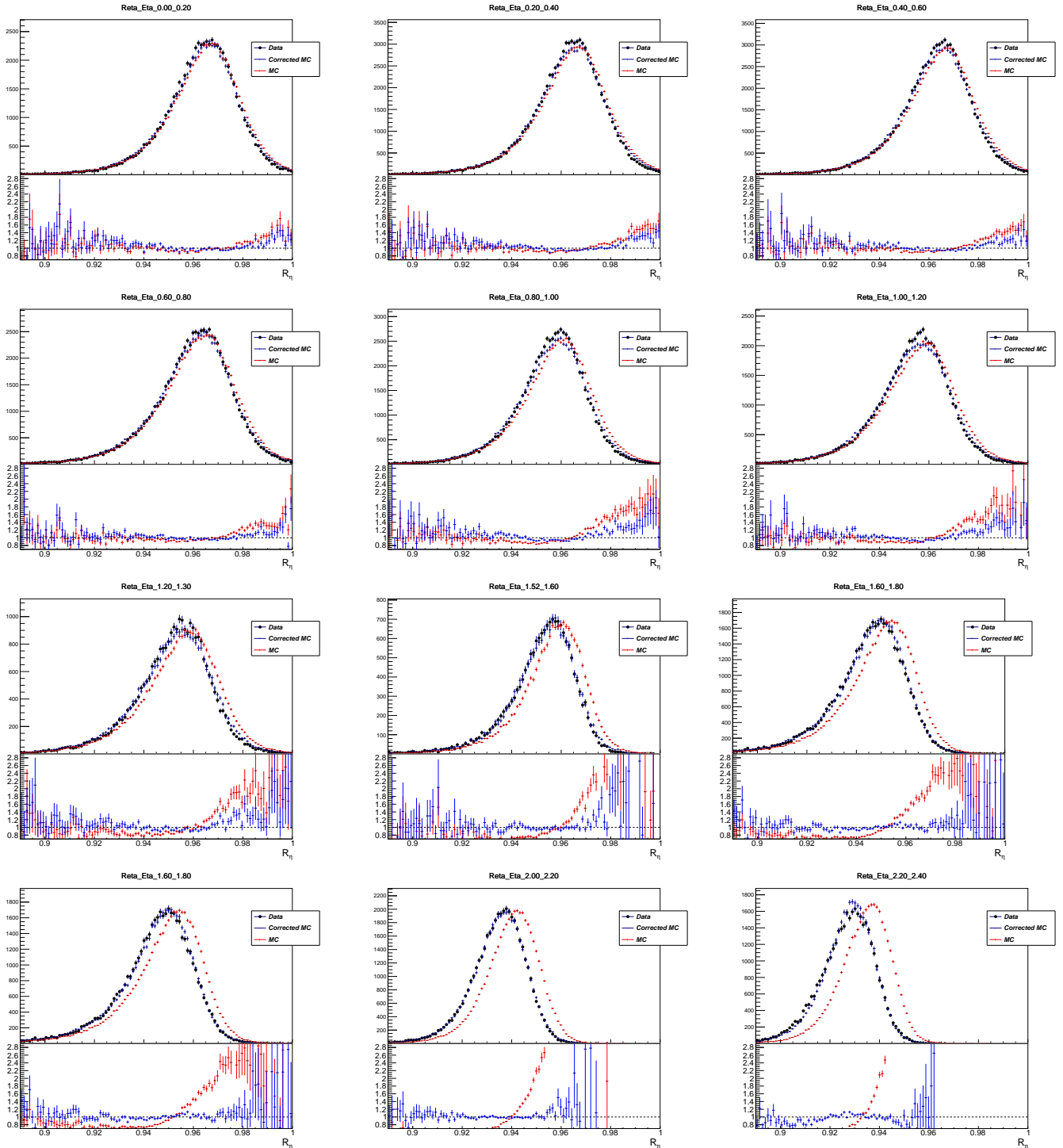


Figure 516: Reta 2

- 879 [4] “Electron reconstruction and identification efficiency measurements with the ATLAS detector
 880 using the 2011 LHC proton-proton collision data. Electron reconstruction and identification effi-
 881 ciency measurements with the ATLAS detector using the 2011 LHC proton-proton collision data”.

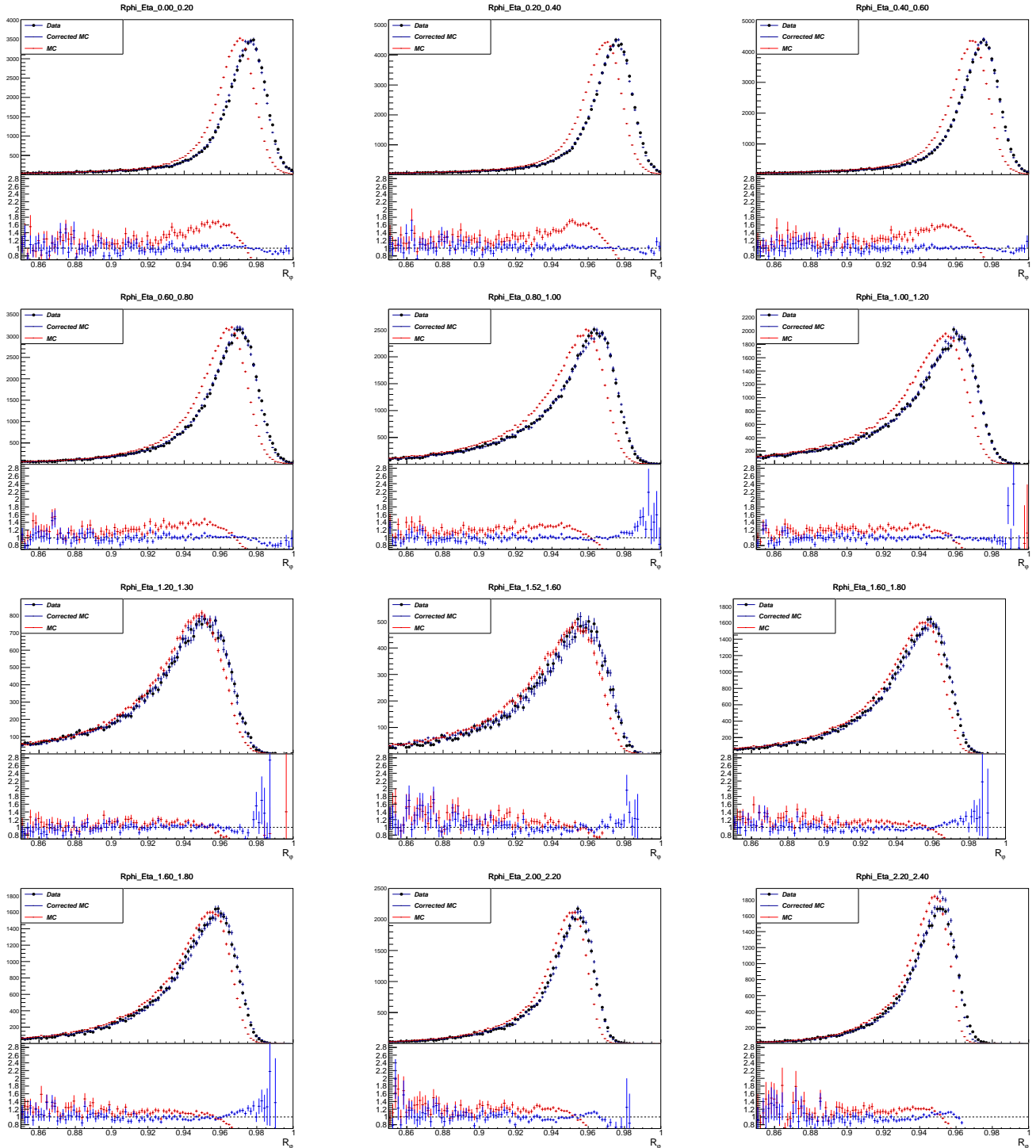


Figure 517: Rphi in all eta slices

In: Eur. Phys. J. C CERN-PH-EP-2014-040. CERN-PH-EP-2014-040 (Apr. 2014). Comments: 38 pages plus author list (62 pages total), 20 figures, 4 tables, submitted to JHEP, All figures including auxiliary figures are available at <https://atlas.web.cern.ch/Atlas/GROUPS/PHYSICS/PAPERS/EPIC/ATLAS-2014-040/>

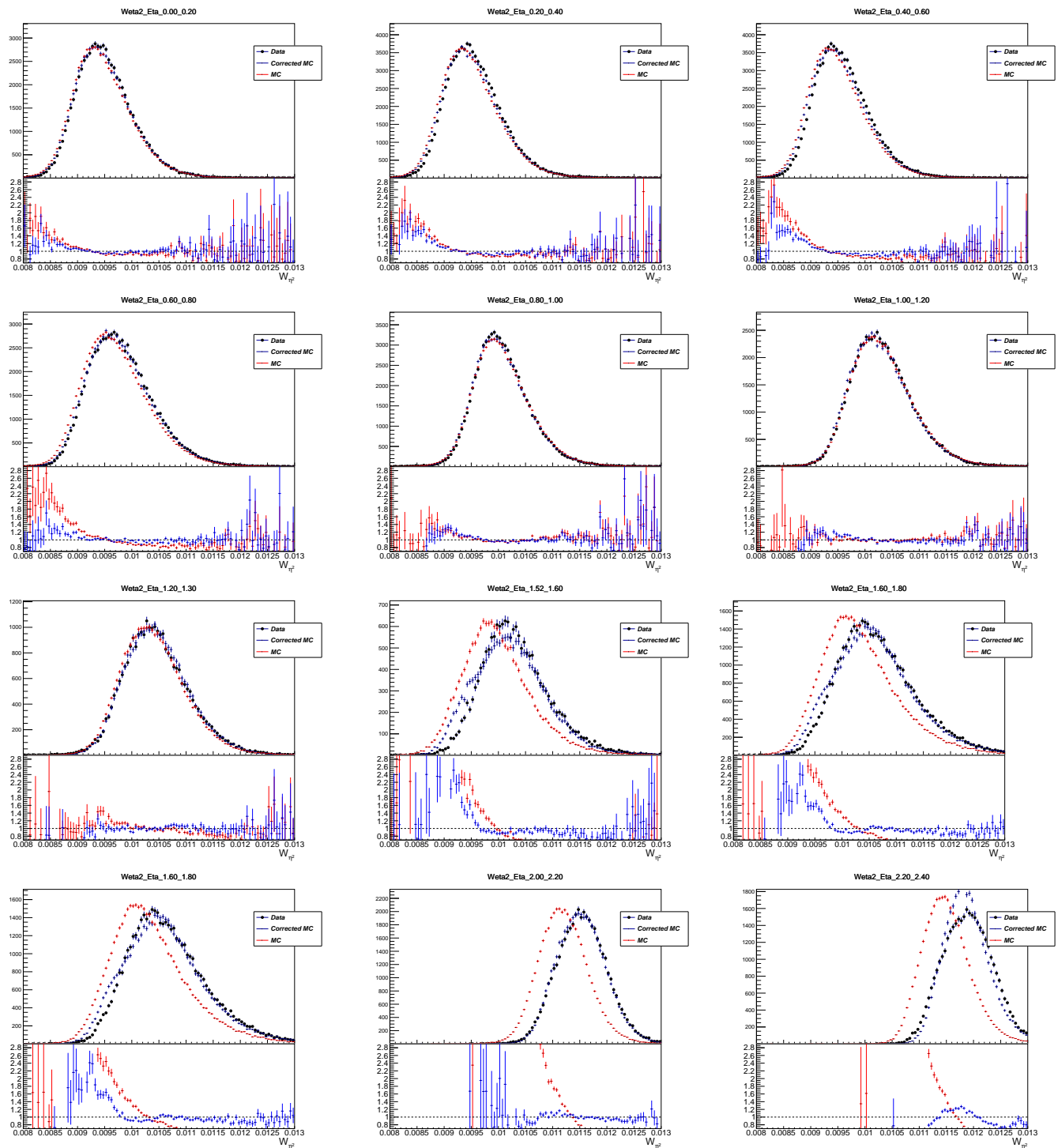


Figure 518: Reta 2

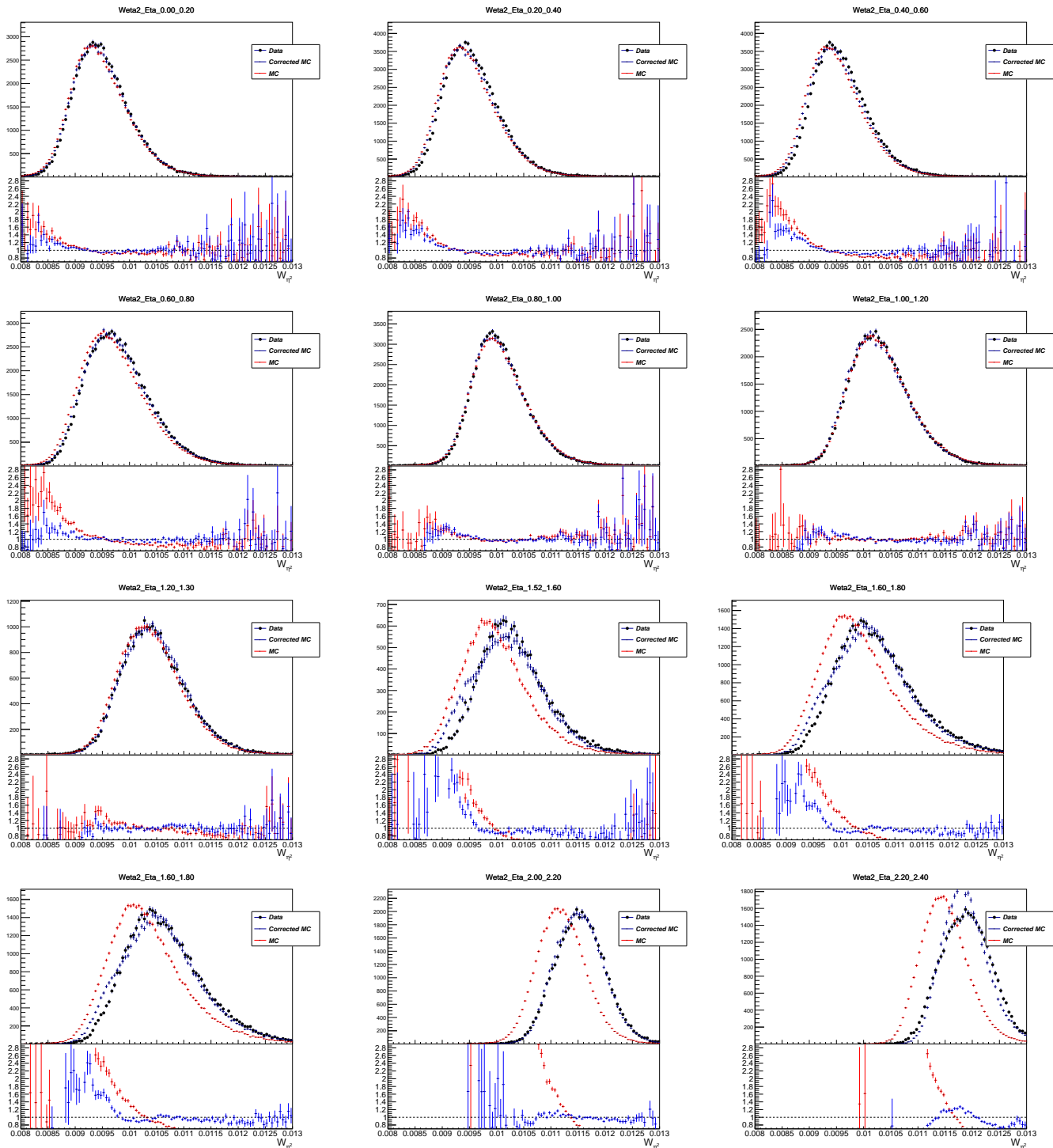


Figure 519: Reta 2

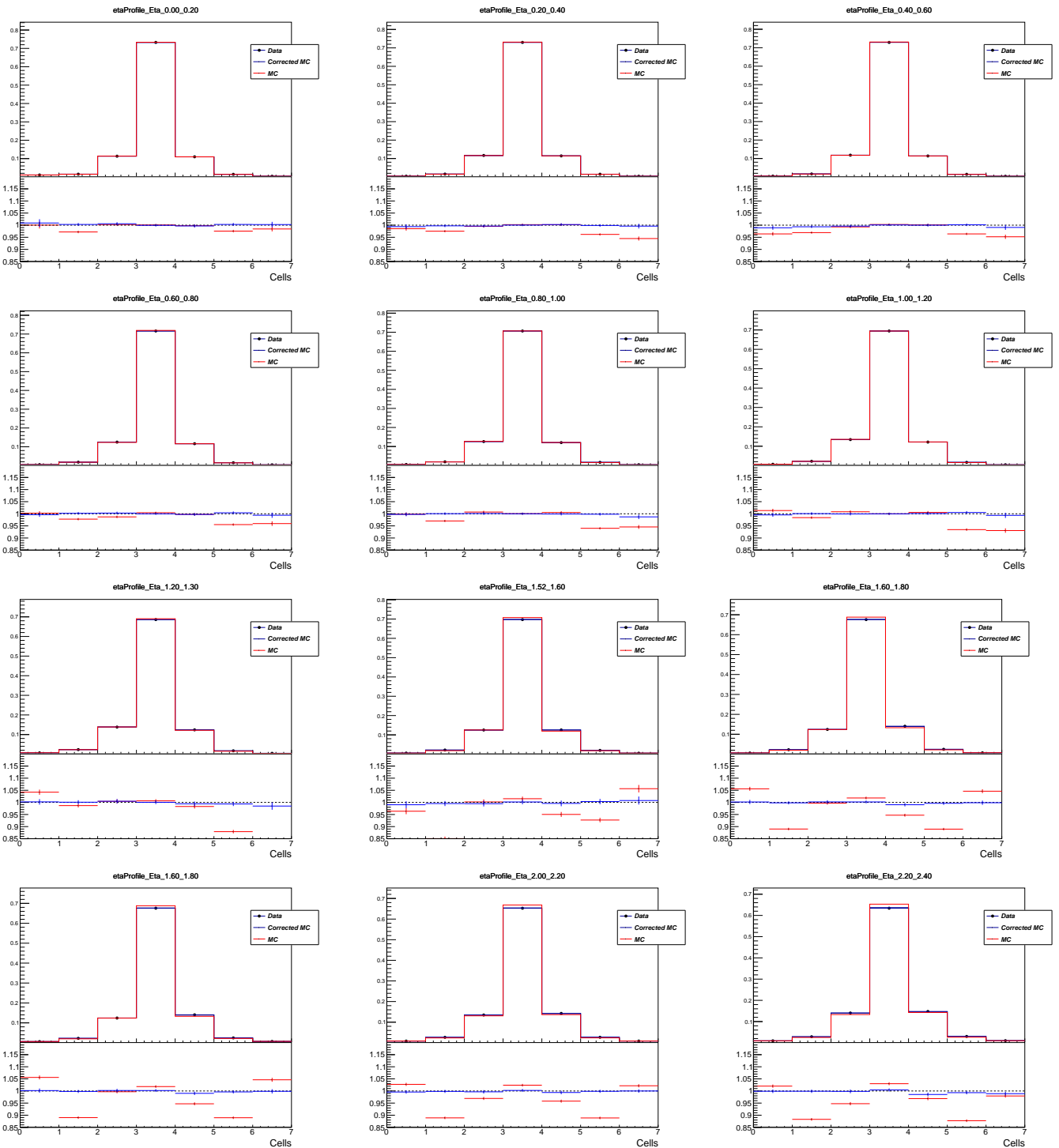


Figure 520: Reta 2

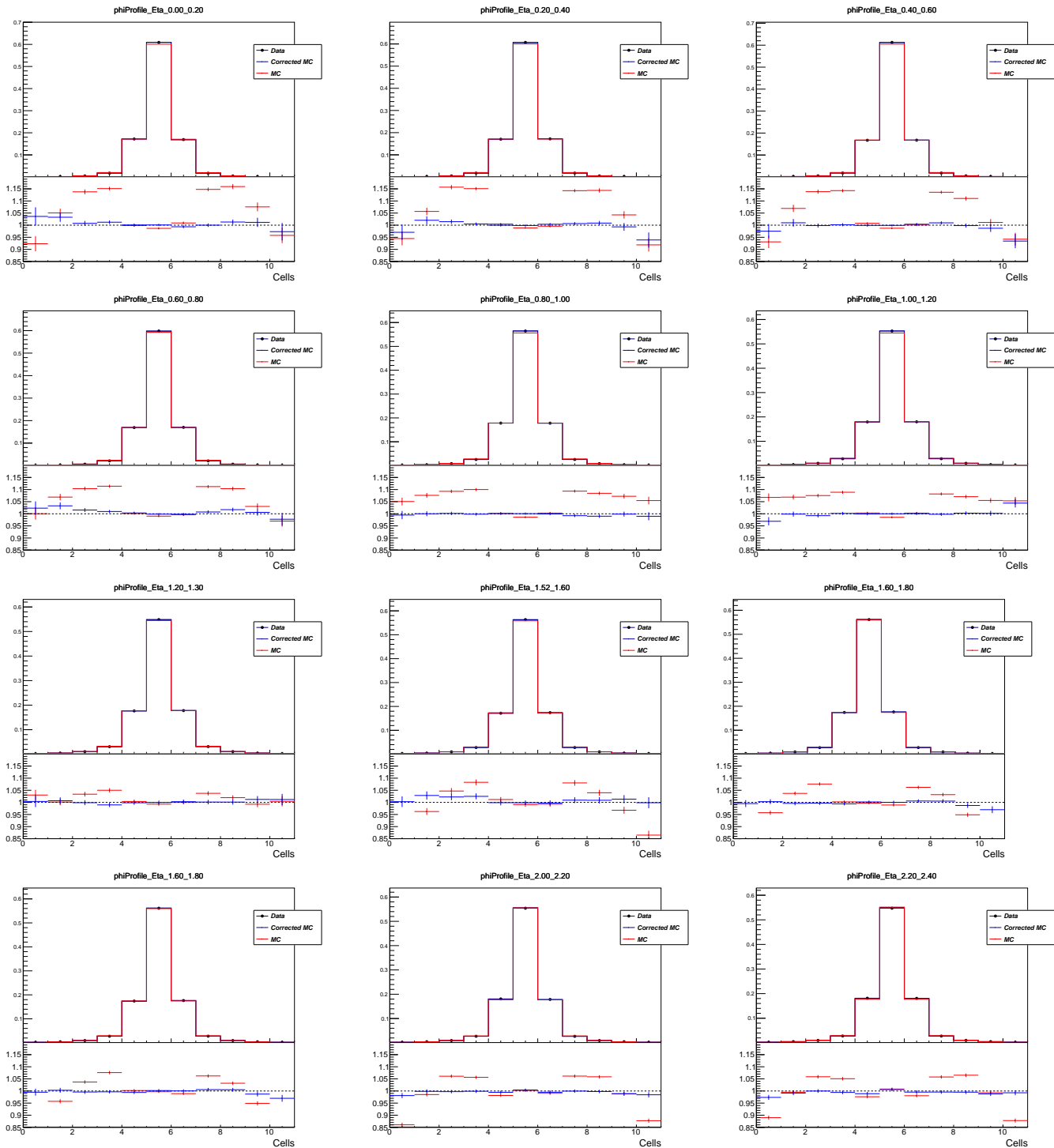


Figure 521: Reta 2

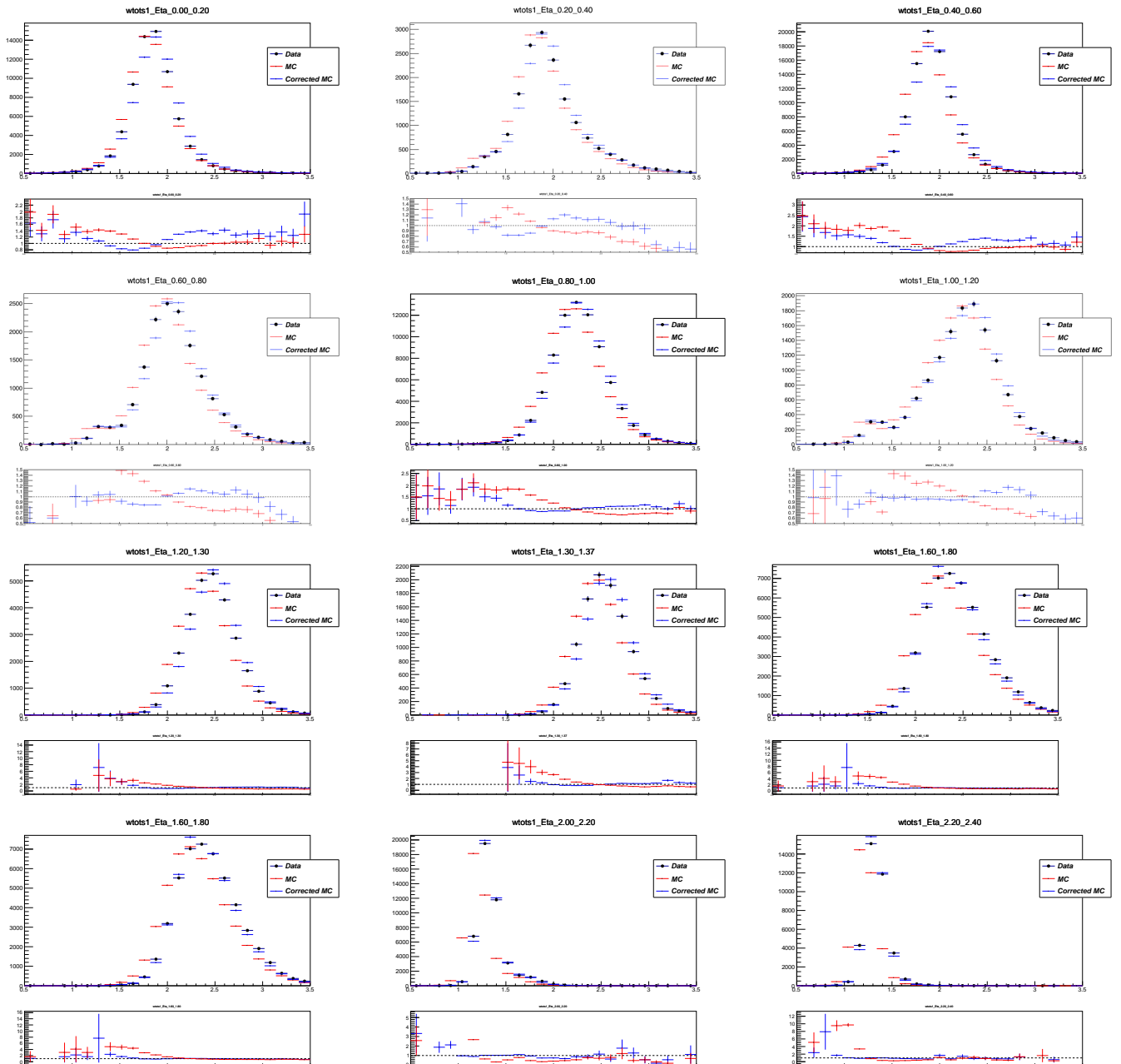


Figure 522: Reta 2